

Sheet beam model for intense space charge: Application to Debye screening and the distribution of particle oscillation frequencies in a thermal equilibrium beam

Steven M. Lund* and Alex Friedman†

Lawrence Livermore National Laboratory, Livermore, California 94550, USA

Guillaume Bazouin‡

Lawrence Berkeley National Laboratory, Berkeley, California 94720, USA

(Received 10 January 2011; published 2 May 2011)

A one-dimensional Vlasov-Poisson model for sheet beams is reviewed and extended to provide a simple framework for analysis of space-charge effects. Centroid and rms envelope equations including image-charge effects are derived and reasonable parameter equivalences with commonly employed 2D transverse models of unbunched beams are established. This sheet-beam model is then applied to analyze several problems of fundamental interest. A sheet-beam thermal equilibrium distribution in a continuous focusing channel is constructed and shown to have analogous properties to two- and three-dimensional thermal equilibrium models in terms of the equilibrium structure and Debye screening properties. The simpler formulation for sheet beams is exploited to explicitly calculate the distribution of particle oscillation frequencies within a thermal equilibrium beam. It is shown that as space-charge intensity increases, the frequency distribution becomes broad, suggesting that beams with strong space-charge can have improved stability relative to beams with weak space-charge.

DOI: [10.1103/PhysRevSTAB.14.054201](https://doi.org/10.1103/PhysRevSTAB.14.054201)

PACS numbers: 29.27.Bd, 41.75.-i, 52.59.Sa

I. INTRODUCTION

Analysis of self-consistent space-charge effects in beams is notoriously difficult due to the nonlinear structure of the Vlasov-Poisson models for realistic, smooth distribution functions. Even the equilibrium structure is generally highly nonlinear which complicates the analysis of the stability and evolution of collective wave perturbations evolving on the equilibrium. Because of this situation, large-scale numerical simulations play a central role in the analysis of charged particle beams. Nevertheless, even when only tractable in idealized limits, problems amenable to analytic analysis increase our understanding of equilibrium and stability properties which in turn helps in interpreting and guiding experiments and/or numerical simulations of more realistic system models.

One-dimensional (1D) sheet-beam models have been applied in the analysis of microwave devices and free-electron lasers [1–5]. 1D sheet-beam models have also been exploited as a simplified framework to gain insight into higher-dimensional models of beams in particle accelerators—particularly on difficult space-charge effects. Sacherer applied a self-consistent, 1D

Kapchinskij-Vladimirskij (KV) model for a uniform density beam to analyze equilibrium and stability properties and applied his results to model space-charge induced effects on resonances in rings [6]. Various studies have applied and extended Sacherer’s pioneering work in interpreting space-charge resonance effects in rings [7–9]. Anderson showed that in a cold, laminar beam limit all initial density perturbations on a uniform density sheet beam are transferred to velocity space in a quarter plasma oscillation period [10]; he also estimated emittance growth rates due to centroid displacements using a sheet-beam model [11]. Analytic descriptions of collective modes in sheet beams have been derived for a continuously focused waterbag (i.e., uniform phase-space) distribution by Startsev and Davidson [12] and by Okamoto and Yokoya for approximate waterbag distributions in both continuous and periodic focusing [8,13]. Davidson *et al.* also analyzed a waterbag distribution in periodic focusing channels in terms of the evolution of the phase-space boundary [14].

In spite of this success in sheet-beam modeling, an issue of concern stems from the Coulomb force being radically different in physical 3D (inverse distance squared), 2D transverse cylindrical (inverse radial distance), and 1D slab (constant; long range) geometries suggesting the possibility of nonphysical collective interactions in the lower-dimensional models. However, it is well known that in 2D beam and plasma systems Debye screening leads to closely similar characteristic transverse collective effects relative to 3D models in spite of the very different Coulomb interaction in 2D and 3D. Here, we first analyze a thermal equilibrium distribution for a continuously focused sheet

*smlund@llnl.gov

†gbazouin@lbl.gov

‡af@llnl.gov

Published by the American Physical Society under the terms of the Creative Commons Attribution 3.0 License. Further distribution of this work must maintain attribution to the author(s) and the published article’s title, journal citation, and DOI.

beam and show that it has surprisingly similar features to higher-dimensional thermal equilibrium models. Then the sheet-beam thermal equilibrium is applied to show that the same characteristic Debye screening is produced in the 1D model as in 3D, thereby supporting the viability of the 1D model because equivalent Debye screening in 1D should lead to similar collective interactions to those in the physical 3D model. The simplicity of the sheet-beam thermal equilibrium model is also exploited to explicitly calculate the distribution of particle oscillation frequencies within the equilibrium beam. The influence of space-charge in broadening of the frequency distribution is parametrically quantified. These large frequency spreads help explain the surprising degree of stability observed in the transport of high intensity beams in both laboratory experiments and simulations.

The organization of this paper is the following. In Sec. II we review and extend a 1D sheet-beam model which can be exploited to more simply analyze a wide variety of beam transport problems with intense space-charge. A Vlasov model and both equilibrium and concavity-based distribution stability in continuous focusing are briefly reviewed (Sec. II A), centroid and envelope equations are derived and rms equivalency is discussed (Sec. II B), and simple parametric equivalences to higher-dimensional beam models are established (Sec. II C). The sheet-beam model is then applied to analyze a thermal equilibrium beam in a continuous focusing channel in Sec. III. The equilibrium density/potential and distribution structure are parametrically illustrated as space-charge intensity is varied (Sec. III A). Debye screening of a test charge inserted in the equilibrium beam is studied (Sec. III B). The simple structure of the equilibrium is exploited to explicitly calculate the distribution of particle oscillation frequencies within the sheet beam including linear applied focusing and nonlinear defocusing space-charge forces (Sec. III C). Concluding discussions in Sec. IV frame the context and usefulness of results analyzed.

II. SHEET-BEAM MODEL

We employ a sheet-beam model in a rectangular x, y, z coordinate system to represent an axially thin, transverse slice of an unbunched ($\partial/\partial z = 0$) charged particle beam composed of a single species of particles of charge q and rest mass m . The slice propagates with velocity $\beta_b c = \text{const}$ and relativistic gamma factor $\gamma_b = \sqrt{1 - \beta_b^2} = \text{const}$ along the axial (z) direction. Here, c is the speed of light *in vacuo*. The independent timelike coordinate is s , which represents the axial coordinate of a reference particle of the beam along the design orbit in the machine. The beam is modeled by a superposition of charge sheets which are distributed in x and uniform in y and z . The beam phase space is described by spatial coordinate x and the angle x' that the sheet particles

make relative to the longitudinal axis of the machine. Primes denote derivatives with respect to s , and in the paraxial approximation $x' \simeq v_x/(\beta_b c)$, where v_x is the x velocity of the sheet. Any y' dependence is dynamically irrelevant and is suppressed for notational clarity. The sheet particles evolve according to the single-particle Hamiltonian

$$H = \frac{1}{2}x'^2 + \frac{1}{2}\kappa x^2 + \frac{q\phi}{m\gamma_b^3\beta_b^2c^2}, \quad (1)$$

with equations of motion

$$\begin{aligned} \frac{d}{ds}x &= \frac{\partial H}{\partial x'} = x', \\ \frac{d}{ds}x' &= -\frac{\partial H}{\partial x} = -\kappa x - \frac{q}{m\gamma_b^3\beta_b^2c^2} \frac{\partial \phi}{\partial x}. \end{aligned} \quad (2)$$

Here, $\kappa(s)$ is the focusing function of the lattice, which is taken to be a prescribed function of s , and ϕ is the electrostatic potential given by the transverse 1D Poisson equation

$$\frac{\partial^2}{\partial x^2}\phi = -\frac{q}{\epsilon_0}n, \quad (3)$$

where $n(x, s)$ is the number density of beam particles. The Poisson equation is solved subject to appropriate boundary conditions. SI units are employed and ϵ_0 is the permittivity of free space.

In contrast to higher-dimensional cases, the 1D Poisson equation (3) for a sheet beam can be fully solved analytically. The one-dimensional beam density n can be thought of as a superposition of sheet charges. Taking in free space, $qn = \sum_s \delta(x - x_s)$ where $\sum_s = \text{const}$ is a surface charge density, $x = x_s$ is the x coordinate of the sheet charge, and $\delta(x)$ a Dirac-delta function, yields $-\partial\phi/\partial x = \text{sgn}(x - x_s)\sum_s/(2\epsilon_0)$, where $\text{sgn}(x) = \pm 1$ denotes the sign of x . Note that in contrast to the field produced by point charges in 2D and 3D systems, the 1D field is long range and does not fall off with distance from the charge source. Using this point source result, the *direct field* in free space is obtained by linear superposition of sheet charges to the left and right of x giving

$$-\frac{\partial\phi}{\partial x} = \frac{q}{2\epsilon_0} \left[\int_{-\infty}^x d\tilde{x}n(\tilde{x}) - \int_x^{\infty} d\tilde{x}n(\tilde{x}) \right] = \frac{qN_x}{\epsilon_0} - \frac{qN}{2\epsilon_0}. \quad (4)$$

Here,

$$N_x \equiv \int_{-\infty}^x d\tilde{x}n(\tilde{x}) \quad (5)$$

is the density integrated to the left of x (s dependence of n is suppressed for notational simplicity). We denote the integrated density (number of particles per unit surface area of the beam) by

$$N \equiv \lim_{x \rightarrow \infty} N_x = \text{const}, \quad (6)$$

which is constant since particles are neither created or destroyed. For future applications note that

$$n = \frac{\partial N_x}{\partial x}. \quad (7)$$

Without loss of generality, a potential reference of $\phi(x=0) = 0$ can be taken while integrating Eq. (4) with respect to x to express the direct field potential in free space as

$$\phi = -\frac{q}{\epsilon_0} \int_0^x d\tilde{x} N_x(\tilde{x}) + \frac{qN}{2\epsilon_0} x. \quad (8)$$

For the special case of a sheet beam with a symmetric density profile about $x=0$ satisfying $n(x) = n(-x)$, $N_x = N/2 + \int_0^x d\tilde{x} n(\tilde{x})$ and the free-space field and potential solutions in Eqs. (4) and (8) reduce to

$$-\frac{\partial \phi}{\partial x} = \frac{q}{\epsilon_0} \int_0^x d\tilde{x} n(\tilde{x}), \quad \phi = \frac{q}{\epsilon_0} \int_0^x d\tilde{x} \int_0^{\tilde{x}} d\tilde{x}' n(\tilde{x}'). \quad (9)$$

For the case of a sheet beam focused between conducting aperture plates (see Fig. 1) at $x = x_{pl}$ and $x = x_{pr}$ which are held at potentials $\phi = \phi_l$ and $\phi = \phi_r$, respectively, the Poisson equation (3) can be integrated from the left boundary at $x = x_{pl}$ with $\frac{\partial \phi}{\partial x}|_{x=x_{pl}}$ undetermined and

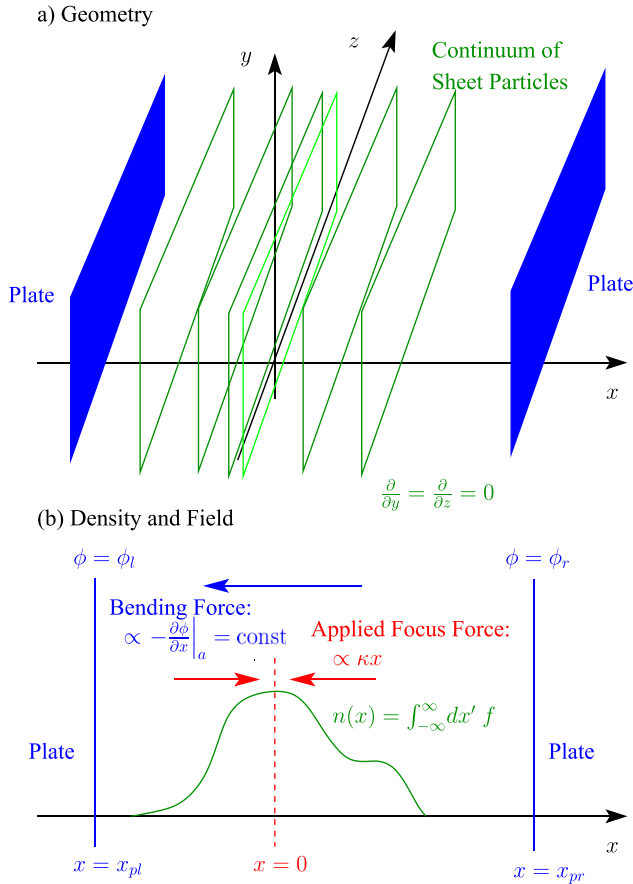


FIG. 1. Schematic of 1D sheet beam (a) geometry with biased conducting plates and (b) density projection and fields.

$\phi(x = x_{pl}) = \phi_l$. Then $\frac{\partial \phi}{\partial x}|_{x=x_{pl}}$ can be calculated by requiring $\phi(x = x_{pr}) = \phi_r$ which gives

$$-\frac{\partial \phi}{\partial x} = -\frac{\phi_r - \phi_l}{x_{pr} - x_{pl}} - \frac{q}{\epsilon_0(x_{pr} - x_{pl})} \int_{x_{pl}}^{x_{pr}} dx N_x - \frac{qN_x}{\epsilon_0}, \quad (10)$$

$$\phi = \phi_l + \left(\phi_r - \phi_l + \frac{q}{\epsilon_0} \int_{x_{pl}}^{x_{pr}} dx N_x \right) \frac{x - x_{pl}}{x_{pr} - x_{pl}} - \frac{q}{\epsilon_0} \int_{x_{pl}}^x d\tilde{x} N_x(\tilde{x}).$$

In the finite geometry solution above, the free-space forms of N_x and N defined in Eqs. (5) and (6) are replaced by $N_x = \int_{x_{pl}}^x d\tilde{x} n(\tilde{x})$ and $N = N_{x=x_{pr}} = \int_{x_{pl}}^{x_{pr}} d\tilde{x} n(\tilde{x})$. Provided that no particles are lost to the plates during the beam evolution, $N = \text{const}$. Comparing the free-space solution (4) and the finite geometry solution (10) for $-\partial \phi / \partial x$, we can resolve the field of the finite geometry system as

$$-\frac{\partial \phi}{\partial x} = -\frac{\partial \phi}{\partial x} \Big|_d - \frac{\partial \phi}{\partial x} \Big|_a - \frac{\partial \phi}{\partial x} \Big|_i, \quad (11)$$

where

$$-\frac{\partial \phi}{\partial x} \Big|_d \equiv \frac{qN_x}{\epsilon_0} - \frac{qN}{2\epsilon_0},$$

$$-\frac{\partial \phi}{\partial x} \Big|_a \equiv -\frac{\phi_r - \phi_l}{x_{pl} - x_{pr}} = \text{const}, \quad (12)$$

$$-\frac{\partial \phi}{\partial x} \Big|_i \equiv -\frac{q}{\epsilon_0(x_{pr} - x_{pl})} \int_{x_{pl}}^{x_{pr}} dx N_x + \frac{qN}{2\epsilon_0},$$

are identified as the (d) direct or free space, (a) applied, and (i) induced image-charge contributions to the solution. The applied field $-\frac{\partial \phi}{\partial x}|_a$ is spatially uniform in x and can be interpreted for $\phi_l \neq \phi_r$ (i.e., when nonzero) as a dispersionless bending or deflection field. The net image field $-\frac{\partial \phi}{\partial x}|_i$ is spatially uniform and can be shown to be zero when the density profile of the beam is symmetric about the geometric center of the aperture. In spite of the long-range 1D field structure, the image field becomes weak when the statistical center of the beam remains near (in a fractional sense) to the geometric center between the plates at $x = (x_{pl} + x_{pr})/2$. These points are illustrated clearly in the centroid equation of motion derived for a uniform density beam in Sec. II B.

For future applications, employing Eq. (2) and the field resolution in Eq. (11), the equation of motion of a general particle can be expressed as

$$x'' + \kappa x = -\frac{q}{m\gamma_b^3 \beta_b^2 c^2} \left(\frac{\partial \phi}{\partial x} \Big|_d + \frac{\partial \phi}{\partial x} \Big|_a + \frac{\partial \phi}{\partial x} \Big|_i \right), \quad (13)$$

with the direct, applied, and image field components specified in Eq. (12). For the case of a sheet beam in free space, the applied and image components are set to zero.

A. Vlasov-Poisson system and continuous focusing equilibria

In the continuum approximation, particle collisions are neglected and the beam evolution is modeled by a single-particle distribution function $f(x, x', s)$ which evolves according to the Vlasov equation:

$$\left\{ \frac{\partial}{\partial s} + \frac{\partial H}{\partial x'} \frac{\partial}{\partial x} - \frac{\partial H}{\partial x} \frac{\partial}{\partial x'} \right\} f(x, x', s) = 0. \quad (14)$$

Within the context of the Vlasov model, the number density n in Poisson's equation (3) is smooth and with normalization choices taken is related to f by

$$n = \int_{-\infty}^{\infty} dx' f. \quad (15)$$

The Vlasov equation (14) with the Hamiltonian in Eq. (1) and electric field solution $-\partial\phi/\partial x$ (including self-direct and image terms as well as possibly an applied bending term when $\phi_l \neq \phi_r$) specified by Eqs. (10) and (15) determine the evolution of the distribution $f(x, x', s)$ in s from a non-negative initial function specified at the initial coordinate $s = s_i$ [i.e. $f(x, x', s = s_i) \geq 0$]. The simplicity of this 1D Vlasov model together with the fully analytic field solution not only enables considerable progress in analytical analysis of beam physics problems, but it can also be exploited as a simple test bed to develop numerical simulation methods—particularly for direct Vlasov simulations [15].

The focusing function $\kappa(s)$ can be related to applied linear electric or magnetic focusing field components using standard formulas from higher-dimensional models (see Refs. [16–19] and the parametric equivalence discussion in Sec. II C). Electric (including continuous focusing) optics cannot be fully consistent with the 1D model geometry assumed and vacuum transport. Nevertheless, they can be applied as additional, idealized imposed forces with consistent coupling strength from the higher-dimensional models. For the special case of a periodic lattice, the function $\kappa(s)$ is periodic with lattice period L_p , i.e., $\kappa(s + L_p) = \kappa(s)$. In this case, it is convenient to measure the strength of κ with the single-particle phase advance per lattice period σ_0 , which can be calculated as [20]

$$\cos\sigma_0 = \frac{1}{2} \text{Tr} \mathbf{M}(s_i + L_p | s_i). \quad (16)$$

Here,

$$\mathbf{M}(s | s_i) = \begin{pmatrix} C(s | s_i) & S(s | s_i) \\ C'(s | s_i) & S'(s | s_i) \end{pmatrix} \quad (17)$$

denotes the 2×2 transfer matrix from axial coordinate s_i to s , $\text{Tr} \mathbf{M}$ denotes the trace of \mathbf{M} , and the $C(s_i | s)$ and $S(s_i | s)$ are cosine-like and sine-like principal orbit functions satisfying

$$F''(s | s_i) + \kappa(s) F(s | s_i) = 0, \quad (18)$$

with F representing C or S and the equation is solved subject to the initial conditions $C(s_i | s_i) = 1$, $C'(s_i | s_i) = 0$, and $S(s_i | s_i) = 0$, $S'(s_i | s_i) = 1$. For periodic lattices, the focusing function κ is generally chosen sufficiently weak with $(1/2)|\text{Tr} \mathbf{M}(z_i + L_p | z_i)| \leq 1$ for the single-particle orbits to be stable.

Analogously to higher-dimensional cases [16,18,19,21], the continuous focusing model with

$$\kappa = k_{\beta 0}^2 = \text{const} \quad (19)$$

is an idealization which can be applied to further simplify the sheet-beam model. In this case the particle phase advance σ_0 and lattice period L_p are arbitrary and all particle orbits moving in the presence of the applied focusing field are stable.

Any positive-definite distribution function $f(\{C_i\})$ formed from a set of constants of the motion $\{C_i\}$ of the single-particle equations of motion (13) produces a valid “equilibrium” solution to the Vlasov equation. Self-consistency requires that $f(\{C_i\})$ generates the electric field $-\partial\phi/\partial x$ required for validity of the $\{C_i\}$. Generally, this is a highly nontrivial constraint. However, for continuous focusing with $\phi_l = \phi_r$ (i.e., no bending), any choice of function $f(H)$ with $f(H) \geq 0$ generates a stationary ($\partial/\partial s = 0$) equilibrium beam because H is a single-particle constant of the motion in this situation.

Global conservation constraints of the 1D Vlasov-Poisson system can be applied as in higher-dimensional models to bound perturbations [22–25]. For systems where particles are not lost, the generalized entropy constraint associated with the Vlasov equation,

$$U_G = \int_{x_{pl}}^{x_{pr}} dx \int_{-\infty}^{\infty} dx' G(f) = \text{const}, \quad (20)$$

applies for any choice of differentiable function $G(f)$ satisfying $G(f \rightarrow 0) = 0$ provided that $f(x' \rightarrow \pm\infty) = 0$ and $f(x = x_{pl}, x_{pr}) = 0$. A special case of Eq. (20) with $G(f) = qf$ is charge conservation, i.e., $qN = q \int_{x_{pl}}^{x_{pr}} dx \int_{-\infty}^{\infty} dx' f = \text{const}$. For the special case of continuous focusing with $\kappa = k_{\beta 0}^2 = \text{const}$ and ϕ_l and ϕ_r constants (i.e., a continuous bend), the sum of the kinetic, applied potential, and electric field energies are constant, which can be expressed as

$$\begin{aligned} U_{\mathcal{E}} = & \int_{x_{pl}}^{x_{pr}} dx \int_{-\infty}^{\infty} dx' \left\{ \frac{1}{2} x'^2 + \frac{1}{2} k_{\beta 0}^2 x'^2 \right\} f \\ & + \frac{\epsilon_0}{2m\gamma_b^3 \beta_b^2 c^2} \int_{x_{pl}}^{x_{pr}} dx \left| \frac{\partial \phi}{\partial x} \right|^2 + \frac{\epsilon_0}{m\gamma_b^2 \beta_b^2 c^2} \\ & \times \left[\phi_r \frac{\partial \phi}{\partial x} \Big|_{x=x_{pr}} - \phi_l \frac{\partial \phi}{\partial x} \Big|_{x=x_{pl}} \right] = \text{const}. \end{aligned} \quad (21)$$

This result is derived in Appendix A where it is also shown that the last term on the left-hand side is associated with energy provided by an external source used to hold the

plates at $x = x_{pl}, x_{pr}$ at potentials $\phi = \phi_l, \phi_r$. Also in Appendix A, the expected result is shown that if $\phi_l = \phi_r$ (possibly varying in s), then Eq. (21) applies without the external source term. Paralleling methods developed for 2D and 3D beams in Refs. [22,24], Eqs. (20) and (21) can be applied to continuously focused sheet-beam equilibria without bending ($\phi_l = \phi_r$) to bound perturbations and show that any equilibrium distribution $f(H)$ that is a monotonic decreasing function of H [i.e., $df(H)/dH \leq 0$] is stable to both small and large amplitude perturbations. For infinite systems (free space), the 1D field-energy term $\propto \int_{-\infty}^{\infty} dx |\partial\phi/\partial x|$ in Eq. (21) diverges. However, analogously to the case in 2D, this divergence can be regularized (i.e., an appropriate infinite constant subtracted) to allow bounding of perturbations to show that sheet-beam equilibria in free space with $df(H)/dH \leq 0$ are stable.

For future use, we denote distribution averages in the Vlasov theory by

$$\langle \cdots \rangle = \frac{1}{N} \int_{x_{pl}}^{x_{pr}} dx \int_{-\infty}^{\infty} dx' \cdots f. \quad (22)$$

Averages of a quantity $g(x, s)$ which is independent of x' can be calculated using $n = \partial N_x / \partial x$ [Eq. (7)] to obtain

$$\langle g \rangle = \frac{1}{N} \int_{x_{pl}}^{x_{pr}} dx g \frac{\partial N_x}{\partial x}. \quad (23)$$

For some particular choices of g , partial integration can be exploited to further simplify Eq. (23).

B. Centroid and envelope equations and the rms-equivalent beam

For present purposes we make no assumptions on the structure of the sheet-beam distribution f and define phase-space coordinates with respect to the center of mass (centroid) $\langle x \rangle$ by

$$\tilde{x} \equiv x - \langle x \rangle, \quad \tilde{x}' \equiv x' - \langle x' \rangle. \quad (24)$$

To derive an equation of motion for the sheet-beam centroid

$$X \equiv \langle x \rangle, \quad (25)$$

the particle equation of motion (13) is averaged to obtain

$$\begin{aligned} X'' + \kappa X &= -\frac{q}{m\gamma_b^3\beta_b^2c^2} \left[\frac{\partial\phi}{\partial x} \Big|_a + \frac{\partial\phi}{\partial x} \Big|_i \right] \\ &= -\frac{q}{m\gamma_b^3\beta_b^2c^2} \left[\frac{\phi_r - \phi_l}{x_{pl} - x_{pr}} + \frac{q}{\epsilon_0(x_{pl} - x_{pr})} \right. \\ &\quad \left. \times \int_{x_{pl}}^{x_{pr}} dx N_x - \frac{qN}{2\epsilon_0} \right]. \end{aligned} \quad (26)$$

There is no direct (free-space) field contribution in Eq. (26). This follows because $\langle \frac{\partial\phi}{\partial x} \Big|_d \rangle = -\frac{q}{\epsilon_0} \langle N_x \rangle + \frac{q}{2\epsilon_0} N = 0$ for any density profile n since $\langle N_x \rangle = \frac{1}{N} \int_{x_{pl}}^{x_{pr}} dx N_x \frac{\partial N_x}{\partial x} = \frac{N}{2}$ provided particles are not lost from the system. The applied

and image terms are independent of x and x' giving $\langle \frac{\partial\phi}{\partial x} \Big|_a \rangle = \frac{\partial\phi}{\partial x} \Big|_a$ and $\langle \frac{\partial\phi}{\partial x} \Big|_i \rangle = \frac{\partial\phi}{\partial x} \Big|_i$. Note that the applied field term effectively acts as an ideal x -plane bending force on the centroid trajectory.

Regardless of the actual distribution of beam space-charge, we define a statistical measure of the half-width of the beam in x about the centroid $x = X$ as

$$x_b = \sqrt{3\langle \tilde{x}^2 \rangle}. \quad (27)$$

This definition is consistent with a uniform density beam with sharp edges about the centroid at $x = X \pm x_b$. The factor of $\sqrt{3}$ in Eq. (27) is a consequence of the 1D geometry and contrasts the familiar factor of 2 in the usual 2D statistical envelope edge definitions [16,18,19,21]. To derive an equation of motion for this ‘‘edge’’ measure of the beam half-width, we first derive an equation of motion for the transformed particle coordinate \tilde{x} by subtracting Eq. (26) from Eq. (13) and applying $\tilde{x} = x - X$ to show that

$$\tilde{x}'' + \kappa\tilde{x} = \frac{q^2}{\epsilon_0 m \gamma_b^3 \beta_b^2 c^2} \left(N_x - \frac{1}{2} N \right). \quad (28)$$

Only the direct (free-space) field is present in this transformed equation of motion because both the applied and image field terms subtract. Differentiating Eq. (27) twice with respect to s and applying the equation of motion (28) leads to the rms envelope equation:

$$x_b'' + \kappa x_b - P \frac{3 \left[\int_{x_{pl}}^{x_{pr}} dx \left(\frac{N_x}{N} \right) - \int_{x_{pl}}^{x_{pr}} dx \left(\frac{N_x}{N} \right)^2 \right]}{x_b} - \frac{\epsilon^2}{x_b^3} = 0. \quad (29)$$

Here,

$$P \equiv \frac{q^2 N}{2\epsilon_0 m \gamma_b^3 \beta_b^2 c^2} = \text{const} \quad (30)$$

is the sheet-beam perveance and

$$\epsilon \equiv 3[\langle \tilde{x}^2 \rangle \langle \tilde{x}'^2 \rangle - \langle \tilde{x}\tilde{x}' \rangle^2]^{1/2} \quad (31)$$

is the rms-edge emittance of the sheet beam. For the 1D sheet beam the perveance P has dimensions 1/length, which contrasts to the typically defined dimensionless perveance of a 2D unbunched beam [16,18,19,21]. Additionally, the rms-edge emittance ϵ is connected to the rms emittance $\epsilon_{x,\text{rms}} \equiv [\langle \tilde{x}^2 \rangle \langle \tilde{x}'^2 \rangle - \langle \tilde{x}\tilde{x}' \rangle^2]^{1/2}$ as $\epsilon = 3\epsilon_{x,\text{rms}}$ with a factor of 3 rather than 4 as in the 2D case due to the structure of the 1D phase space.

Contrasting the equations of motion (26) and (29) for the centroid X and envelope x_b , the fact that the applied field $-\frac{\partial\phi}{\partial x} \Big|_a$ enters only the centroid equation is not surprising since any nonzero applied field acts as an ideal (bending) dipole term. The lack of image contribution in the envelope equation results from the independent of x structure of the induced fields in the 1D geometry. The image term in the centroid equation $[-\frac{\partial\phi}{\partial x} \Big|_i]$ will generally evolve in s with

the form of the density profile n produced by the sheet-beam distribution f . Similarly, in the envelope equation, both the defocusing self-field perveance term ($\propto P$) and the emittance ε will generally evolve in s . Thus, the centroid and envelope equations can only be integrated under additional assumptions or analysis to quantify generally non-constant terms in the equations.

For the special case of a sheet beam with uniform density between sharp edges at $x = X \pm x_b$, we have

$$n(x) = \int_{-\infty}^{\infty} dx' f = \begin{cases} 0, & X + x_b < x < x_{pr}, \\ \hat{n}, & X - x_b < x < X + x_b, \\ 0, & x_{pl} < x < X - x_b, \end{cases} \quad (32)$$

with \hat{n} constant in x but possibly varying in s . Consistent with charge conservation,

$$\hat{n} = \frac{N}{2x_b} \quad (33)$$

with $N = \text{const.}$ Using this density profile the centroid equation (26) reduces to

$$X'' + \kappa X = -\frac{q}{m\gamma_b^3\beta_b^2c^2} \frac{\phi_r - \phi_l}{x_{pr} - x_{pl}} + \frac{2P}{x_{pr} - x_{pl}} \left(X - \frac{x_{pr} + x_{pl}}{2} \right), \quad (34)$$

and

$$\frac{3 \left[\int_{x_{pl}}^{x_{pr}} dx \left(\frac{N_x}{N} \right) - \int_{x_{pl}}^{x_{pr}} dx \left(\frac{N_x}{N} \right)^2 \right]}{x_b} = 1,$$

thereby reducing the envelope equation (29) to simply

$$x_b'' + \kappa x_b - P - \frac{\varepsilon^2}{x_b^3} = 0. \quad (35)$$

Note that Eqs. (34) and (35) are *decoupled* for a uniform density sheet beam with the centroid equation independent of x_b and the envelope equation independent of X . From Eq. (34), the image force acting on the centroid is a linear defocusing force which is zero when the beam is centered in the aperture with $X = \langle x \rangle = (x_{pr} + x_{pl})/2$. Even though self-field forces are long range in 1D, the image force becomes weak when the fractional deviation of X from the aperture center at $(x_{pr} + x_{pl})/2$ is small due to relative values of induced charge on the two plates being closely tuned. Naturally, the image force also becomes weak for small beam perveance P . From Eq. (35), the space-charge defocusing term of a uniform density sheet beam is simply a constant (P). This structure *a posteriori* motivates the choice of numerical coefficients incorporated in the definition of the sheet-beam perveance P in Eq. (30). The constant space-charge defocusing term acting in the envelope equation contrasts forms found in 2D and 3D systems for uniform density beams. In the 2D and 3D cases space-charge strength varies inversely with the beam envelope extent.

Analysis by Sacherer [6] shows that the distribution,

$$f = \frac{N}{2\pi\varepsilon\sqrt{1 - \left(\frac{\tilde{x}}{x_b}\right)^2 - \left(\frac{x_b\tilde{x}' - x_b'\tilde{x}}{\varepsilon}\right)^2}} \times \Theta \left[1 - \left(\frac{\tilde{x}}{x_b}\right)^2 - \left(\frac{x_b\tilde{x}' - x_b'\tilde{x}}{\varepsilon}\right)^2 \right], \quad (36)$$

satisfies the 1D Vlasov-Poisson system consistent with the assumption of uniform beam density in Eq. (32). Here, $\Theta(x)$ is the unit-step function defined by $\Theta(x) = 0$ for $x < 0$, and $\Theta(x) = 1$ for $x > 0$. The distribution (36) is the 1D analog of the well-known 2D KV distribution [16,21,26]. It is straightforward to show that the KV distribution (36) is a function of Courant-Snyder invariants [20,21,27] of the linear equation of motion,

$$\tilde{x}'' + \kappa\tilde{x} - \frac{P}{x_b}\tilde{x} = 0, \quad (37)$$

which describes a particle moving within the uniform density beam (i.e., $|\tilde{x}| < x_b$). Although the sheet-beam KV distribution diverges at the phase-space edge, it does not possess the same degree of singularity (delta function) in phase space as occurs for the 2D KV distribution. The 1D KV distribution (36) is the unique self-consistent distribution that produces a uniform density beam and evolves consistently with the envelope equation (35) with $\varepsilon = \text{const.}$ An interesting feature of the construction in 1D is that it is consistent with image charges because image forces are linear in 1D and are therefore consistent with the preservation of Courant-Snyder invariants. This contrasts the situation for a 2D KV distribution where image forces generally must be neglected [except for cases where boundaries can be chosen for zero net image force such as an axisymmetric ($\partial/\partial\theta = 0$) beam confined within an axisymmetric pipe] for consistency with a KV distribution because the net image force on a particle within the beam generally varies nonlinearly with respect to the proximity of the particle relative to the aperture.

The existence of a self-consistent, uniform density sheet beam satisfying the centroid and envelope equations (34) and (35) motivates construction of an rms-equivalent beam analogously to the well-known 2D case. As in 2D, one can aid the interpretation of a general sheet beam evolving with nonuniform density by replacing the actual sheet-beam distribution f with an ‘‘rms-equivalent’’ KV sheet-beam distribution. The rms-equivalent beam has uniform density with the same species (q, m), energy (β_b), charge (N , or equivalently P), and identical first and second order moments as the nonuniform density beam as summarized in Table I. The rms-equivalent beam will have identical centroid (X, X') and envelope (x_b, x_b') phase-space coordinates, and emittances (ε) as the nonuniform density beam it replaces. The subsequent evolution of the rms-equivalent beam according to the coupled envelope and centroid equations (34) and (35) with constant normalized emittances generally provides a reliable model for the

TABLE I. Sheet-beam rms equivalency with $\tilde{x} = x - \langle x \rangle$ and $\tilde{x}' = x' - \langle x' \rangle$.

Quantity	rms equivalent	Calculated from distribution
Perveance	P	$= q^2 N / (2\epsilon_0 m \gamma_b^3 \beta_b^2 c^2)$
Centroid coordinate	X	$= \langle x \rangle$
Centroid angle	X'	$= \langle x' \rangle$
Envelope coordinate	x_b	$= \sqrt{3\langle \tilde{x}^2 \rangle}$
Envelope angle	x'_b	$= \sqrt{3\langle \tilde{x}\tilde{x}' \rangle} / \sqrt{\langle \tilde{x}^2 \rangle}$
Emittance	ε	$= 3\sqrt{\langle \tilde{x}^2 \rangle \langle \tilde{x}'^2 \rangle} - \langle \tilde{x}\tilde{x}' \rangle^2$

statistical evolution of the real beam *if* nonlinear force effects leading to emittance growth are sufficiently small. The envelope of a space-charge dominated beam will generally be insensitive to modest emittance growth that may result from nonlinear forces because the emittance term ε^2/x_b^3 in the envelope equation is small. Alternatively, the rms-equivalent prescription can be applied as a function of s to aid interpretation of the evolution of the physical beam.

The rms-equivalent beam can be used to form a convenient, dimensionless measure of space-charge strength in a periodic or continuous focusing channel. For a periodic channel with $\kappa(s + L_p) = \kappa(s)$, techniques analogous to those presented in Ref. [21] for 2D beams show that particles moving within an rms-equivalent beam which is *matched* to the focusing channel [i.e., KV rms-equivalent parameters chosen so that the envelope solution to Eq. (35) has the periodicity of the lattice with $x_b(s + L_p) = x_b(s)$] have phase advance

$$\sigma = \varepsilon \int_{s_i}^{s_i + L_p} \frac{ds}{x_b^2} \quad (38)$$

per lattice period. The choice of s_i within the lattice period is arbitrary. The ratio σ/σ_0 can be applied as a convenient, normalized measure of space-charge strength with $\sigma/\sigma_0 \in (0, 1)$ with $\sigma/\sigma_0 \rightarrow 1$ corresponding to a warm beam ($P \ll \varepsilon/x_b^3$) with zero space-charge intensity and $\sigma/\sigma_0 \rightarrow 0$ corresponding to a cold beam ($P \gg \varepsilon/x_b^3$) with maximum space-charge intensity. For the special case of a continuously focused beam with $\kappa = k_{\beta 0}^2 = \text{const}$, the choice of lattice period L_p to measure phase advances is arbitrary, and it can be shown that

$$\frac{\sigma}{\sigma_0} = \sqrt{1 - \frac{P}{k_{\beta 0}^2 x_b^3}}. \quad (39)$$

It is straightforward to show that this result is consistent with the linear equation of motion (37) for any particle evolving within a KV beam.

It is interesting to contrast centroid and envelope oscillations in X and x_b supported by an rms-equivalent sheet beam and contrast results with those found in higher-dimensional models [16–19]. First, for the centroid X , consider the special case of a sheet beam transported without

bending ($\phi_l = \phi_r$) and with an aperture centered about $x = 0$ (applied focus center) with $x_{pr} = -x_{pl} = x_p$. Then the centroid equation (34) takes the form of Hill's equation

$$X'' + \kappa_{\text{eff}} X = 0 \quad (40)$$

with

$$\kappa_{\text{eff}} = \kappa - \frac{P}{x_p}. \quad (41)$$

This equation of motion shows that in this situation the image charges act as a continuous defocusing correction to the applied focusing function κ and therefore the standard treatments from accelerator physics of single-particle orbits moving in a prescribed focusing function $\kappa_{\text{eff}}(s)$ can be applied to describe the centroid orbit [20]. The lack of nonlinear amplitude dependence in the sheet-beam image force results in a stable centroid orbit that does not increase in amplitude as oscillations advance in s (or phase), which is contrary to what is found (typically weak amplitude increases in s) in higher-dimensional models [17–19]. However, the sheet-beam model has a roughly correct image-charge induced shift in the phase advance of centroid oscillations when compared to higher-dimensional models [17–19]. Changes in this simplified centroid analysis due to an asymmetric aperture ($x_{pr} \neq -x_{pl}$) and/or bending forces ($\phi_l \neq \phi_r$) are straightforward to analyze.

Next, envelope oscillations in x_b for a sheet beam can be better understood by carrying out a standard stability analysis taking $x_b = x_{b0} + \delta x_b$ with x_{b0} satisfying the envelope equation (35) in the absence of perturbations (i.e., $\delta x_b = 0$). Assuming $|\delta x_b|/x_{b0} \ll 1$ and expanding Eq. (35) to leading order gives the linearized envelope equation

$$\delta x_b'' + \kappa \delta x_b + 3 \frac{\varepsilon^2}{x_{b0}^4} \delta x_b = 0. \quad (42)$$

Typically, x_{b0} is taken to be the matched solution when applied to a periodic lattice [i.e., for $\kappa(s + L_p) = \kappa(s)$, $x_{b0}(s + L_p) = x_{b0}(s)$]. Note that there is no direct modulation of the space-charge (perveance) term in Eq. (42) as is the case for “quadrupole” symmetry envelope modes found in 2D transverse models of an unbunched beam [17]. The special case of a continuous focusing channel with $\kappa = k_{\beta 0}^2 = \text{const}$ and a matched envelope $x_{b0} = \text{const}$ satisfying $k_{\beta 0}^2 x_{b0} - P - \varepsilon^2/x_{b0}^3 = 0$ further clarifies the correspondence between 1D and 2D model results. Assuming harmonic variations in $\delta x_b \propto e^{iks}$ with $i \equiv \sqrt{-1}$ and k the mode wave number, the linear envelope equation (42) reduces to a dispersion relation showing stable oscillations with relative spatial oscillation frequency

$$\frac{k}{k_{\beta 0}} = \pm \sqrt{1 + \frac{3\varepsilon^2}{k_{\beta 0}^2 x_{b0}^4}} = \pm \sqrt{1 + 3\left(\frac{\sigma}{\sigma_0}\right)^2}. \quad (43)$$

Here, in the second form of the dispersion given, the continuous focusing phase advance formula (39) has been

applied to express the result in terms of σ/σ_0 . Note that the mode frequency variation in σ/σ_0 is identical to the familiar quadrupole mode in 2D [17], thereby showing that the analog of quadrupole envelope mode oscillations can be faithfully modeled in the sheet-beam system. However, the higher frequency “breathing” modes supported in 2D are not found in the sheet-beam model. Analysis presented in Refs. [16,17] can be paralleled to analyze the stability properties of envelope modes supported by a matched sheet beam in a periodic focusing channel.

Finally, it is interesting to illustrate similarities in the sheet-beam model and higher-dimensional beam models with regard to rms emittance evolution. First, we differentiate the rms-edge emittance definition in Eq. (31) with respect to s and apply the equation of motion (28) along with $\langle \tilde{x} \rangle = 0 = \langle \tilde{x}' \rangle$ to show that

$$\frac{d}{ds} \varepsilon^2 = \frac{36P}{N} [\langle \tilde{x}^2 \rangle \langle \tilde{x}' N_x \rangle - \langle \tilde{x} \tilde{x}' \rangle \langle \tilde{x} N_x \rangle]. \quad (44)$$

This result can be shown to be equivalent to a statement that nonlinear components of the direct space-charge field drive rms emittance growth in the sheet-beam model. Analysis in Appendix B shows that for the special case of a symmetric beam [i.e., $n(x) = n(-x)$] in a symmetric geometry without bending (i.e., $x_{pr} = -x_{pl} = x_p$ and $\phi_l = \phi_r = \text{const}$, and consequently $X = 0 = X'$), Eq. (44) can be recast as [10]

$$\frac{d}{ds} \varepsilon^2 = \frac{18}{Nm\gamma_b^3 \beta_b^2 c^2} \langle x^2 \rangle^{3/2} \frac{d}{ds} \left(\frac{W_F}{\langle x^2 \rangle^{1/2}} \right), \quad (45)$$

where

$$\begin{aligned} W_F &\equiv \frac{q^2 N^2 x_p}{4\epsilon_0} - \frac{\epsilon_0}{2} \int_{-x_p}^{x_p} dx \left| \frac{\partial \phi}{\partial x} \right|^2 \\ &= \frac{q^2}{\epsilon_0} \int_0^{x_p} dx N_x (N - N_x) \end{aligned} \quad (46)$$

is a measure of field energy. Note that $W_F = \text{const} - W$, where $W = (\epsilon_0/2) \int_{-x_p}^{x_p} dx |\partial \phi / \partial x|^2$ is the self-field energy per unit area for this geometry. This result is similar to the results obtained for unbunched axisymmetric beams in 2D by Lapostolle, Lee, Wangler, and coauthors in Refs. [28–31]. As is the case in 2D, for fixed charge and envelope half-width $x_b = \sqrt{3\langle \tilde{x}^2 \rangle}$, a uniform density sheet beam is found to minimize W [10], so from $W_F = \text{const} - W$ and Eq. (46), one expects as in 2D beams that symmetric local beam evolutions tending to make the beam density profile less/more uniform will decrease/increase the rms-edge emittance ε . If the effect of emittance evolution is negligible on the mean square beam width $\langle x^2 \rangle$, then Eq. (45) can be integrated to obtain

$$\begin{aligned} \varepsilon^2 - \varepsilon_i^2 &\simeq \frac{18}{Nm\gamma_b^3 \beta_b^2 c^2} \langle x^2 \rangle (W_F - W_{Fi}) \\ &\simeq - \frac{18}{Nm\gamma_b^3 \beta_b^2 c^2} \langle x^2 \rangle (W - W_i), \end{aligned} \quad (47)$$

where subscript i denotes initial values.

C. Parametric equivalences with higher-dimensional beam models

When applying the 1D sheet-beam model to analyze higher-dimensional beam models, it is desirable to employ sheet-beam parameters that are reasonably “equivalent” to the higher-dimensional formulations. A simple equivalence prescription to an unbunched, 2D transverse model of a coasting beam without bending is to set initial ($s = s_i$) sheet-beam parameters as follows:

Trivially, one should employ the same particle species (q, m) and axial velocity (β_b) in the sheet-beam model as the 2D model. For either continuous or quadrupole (magnetic or electric) focusing channels, the applied focusing function κ of the sheet-beam model can be set as

$$\kappa = \kappa_j, \quad (48)$$

where κ_j with $j = x$ or y to represent either the x - or y -plane focusing function κ_x or κ_y of the 2D system. For the case of solenoid focusing and an axisymmetric beam, it is reasonable to take κ_j in Eq. (48) to be the Larmor-frame focusing strength [17,32] of the higher-dimensional model and interpret the sheet-beam model result as if it were in the rotating Larmor frame. Formulas relating the focusing function κ to applied field components for continuous, electric, and magnetic quadrupole, and solenoidal focusing can be found in Refs. [16–19]. Aperture plate distances can be set to the beam pipe radius r_p of the 2D system (i.e., $x_{pr} = -x_{pl} = r_p$) for approximately correct image strengths.

The sheet-beam perveance P [Eq. (30)] can be set from the usual 2D beam dimensionless perveance $Q \equiv q\lambda/(2\pi\epsilon_0 m\gamma_b^3 \beta_b^2 c^2)$ ($\lambda = \text{const}$ here denotes the 2D beam line-charge) by requiring the rms-equivalent uniform density beams in both the sheet beam and the 2D model to have the same characteristic transverse spatial extent and density scale \hat{n} . This results in both systems having the same plasma frequency $\omega_p = [q^2 \hat{n}/(\epsilon_0 m)]^{1/2}$ characteristic of collective effects. For a sheet beam with characteristic extent $x_b = \sqrt{3\langle \tilde{x}^2 \rangle}$ and density $\hat{n} = N/(2x_b)$, and a 2D beam with characteristic radial extent r_b and density $\hat{n} = \lambda/(q\pi r_b^2)$, taking equal densities and $x_b = r_b$ gives an equivalent sheet-beam perveance of

$$P = \frac{2Q}{r_b}. \quad (49)$$

In applying Eq. (49) to 2D systems without x - and y -plane symmetry and 2D rms-equivalent elliptical beam edge radii r_x and r_y , it is reasonable to take $r_b = r_x$ or $r_b = r_y$

to analyze the x - or y -plane, or $r_b = \sqrt{r_x r_y}$ if a plane-average value is preferred for a beam which is not highly elliptical. For the case of a periodic focusing lattice and a matched beam with significant period variation, it is reasonable to replace r_x and r_y by period averages.

In a similar manner to the perveance equivalence, it is reasonable to set the rms-edge emittance $\varepsilon = 3\varepsilon_{x,\text{rms}}$ with $\varepsilon_{x,\text{rms}} = [\langle \tilde{x}^2 \rangle \langle \tilde{x}'^2 \rangle - \langle \tilde{x} \tilde{x}' \rangle^2]^{1/2}$ [see Eq. (31)] of the sheet beam in terms of the usual rms-edge emittance $\varepsilon_x = 4\varepsilon_{x,\text{rms}}$ of the 2D beam with

$$\varepsilon = \varepsilon_x. \quad (50)$$

Note that the difference in edge coefficients of 3 (1D) and 4 (2D) in ε and ε_x result from the differing dimensionality of the transverse phase space. If there are significant x - and y -plane variations in the 2D emittances, then it may be preferable to replace $\varepsilon_x \rightarrow \varepsilon_y$ in the equivalence (50) or replace $\varepsilon_x \rightarrow \sqrt{\varepsilon_x \varepsilon_y}$ depending on whether particular plane or average properties are desired. Similar, but more approximate, equivalences can be developed to the 2D case presented above to apply the sheet-beam model to 3D bunched beams.

Further insight can be achieved by applying the equivalency procedure outlined above to a 2D continuously focused beam with focusing strength $\kappa_x = \kappa_y = k_{\beta 0}^2 = \text{const}$, perveance Q , rms-edge emittances $\varepsilon_x = \varepsilon_y = \text{const}$, and matched envelope radii $r_x = r_y = r_b = \text{const}$. The matched beam envelope equation $k_{\beta 0}^2 r_b - Q/r_b - \varepsilon_x^2/r_b^3 = 0$ (see Ref. [17]) can then be solved for r_b , which is then inserted in the perveance equivalency condition (49) to obtain a simple expression for the equivalent sheet-beam perveance with continuous focusing strength $\kappa = k_{\beta 0}^2$ as

$$P = \frac{2^{3/2} k_{\beta 0} Q}{\sqrt{Q + \sqrt{Q^2 + 4k_{\beta 0}^2 \varepsilon_x^2}}}. \quad (51)$$

In the limit of a space-charge dominated 2D beam, $Q \gg k_{\beta 0} \varepsilon_x$, the equivalency condition (51) reduces to $P/k_{\beta 0} \approx 2\sqrt{Q}$. Conversely, in the limit of an emittance dominated 2D beam, $k_{\beta 0} \varepsilon_x \gg Q$, and the equivalency condition (51) reduces to $P/k_{\beta 0} \approx 2Q/\sqrt{k_{\beta 0} \varepsilon_x}$. It is interesting to point out that, for KV beam distributions in the context of this continuous focusing equivalency, both depressed and undepressed orbits of particles within the sheet beam and along the principal axis of the 2D beam will be the same for the same initial conditions within the beam.

III. THERMAL EQUILIBRIUM SHEET BEAM IN A CONTINUOUS FOCUSING CHANNEL

Thermal equilibrium distributions have been extensively studied in 2D non-neutral plasmas confined in Penning-Malmberg traps [33–35] and continuously focused beams [18,19,21,34,36,37]. Results based on a 1D sheet-beam

model can also be found in the Appendix of Ref. [8]. For a continuously focused ($\kappa = k_{\beta 0}^2 = \text{const}$) sheet beam in free space (without conducting apertures or bending), the thermal equilibrium distribution is given by

$$f(H) = \left(\frac{m\gamma_b \beta_b^2 c^2}{2\pi T} \right)^{1/2} \hat{n} \exp\left(\frac{-m\gamma_b \beta_b^2 c^2 H}{T} \right). \quad (52)$$

Here, $T = \text{const}$ is the thermodynamic temperature (expressed in energy units) in the laboratory frame and $\hat{n} = \text{const}$ is the characteristic density scale. This thermal equilibrium distribution is the special stable ($\partial f / \partial H < 0$) equilibrium that any initial distribution function $f(x, x', s = s_i)$, however complex, will ultimately relax to through collisional effects outside the Vlasov model. Although the time scale of collisional relaxation is typically slow relative to beam residence times in a machine, collective effects and couplings to external errors and noise sources can drive enhanced rates of relaxation. In this regard the sheet-beam thermal distribution (52) can be considered the preferred equilibrium of the system.

A. Equilibrium solution

We analyze properties of the sheet-beam thermal equilibrium distribution (52) exploiting a close analogy to extensively analyzed theory presented in Appendix F of Ref. [21] for the thermal equilibrium of a continuously focused 2D cylindrical beam. First, the local kinetic temperature T_x and beam density n are calculated from Eq. (52) as

$$T_x \equiv m\gamma_b \beta_b^2 c^2 \frac{\int_{-\infty}^{\infty} dx' x'^2 f}{\int_{-\infty}^{\infty} dx' f} = T = \text{const}, \quad (53)$$

$$n \equiv \int_{-\infty}^{\infty} dx' f = \hat{n} e^{-\psi},$$

where

$$\psi \equiv \frac{m\gamma_b \beta_b^2 c^2}{T} \left(\frac{1}{2} k_{\beta 0}^2 x^2 + \frac{q\phi}{m\gamma_b^3 \beta_b^2 c^2} \right). \quad (54)$$

Consistent with the reference choice $\phi(x=0)=0$, $\psi(x=0)=0$, and $\hat{n} = n(x=0)$ is identified as the on-axis density. Note that the local kinetic temperature is spatially uniform—as should be expected with a thermal equilibrium distribution. However, the density n varies in x due to the applied focusing potential ($\propto k_{\beta 0}^2 x^2$) and the self-field potential ϕ , both of which are included in the effective potential ψ .

Using Eqs. (53) and (54), the Poisson equation (3) for thermal equilibrium can be expressed in scaled form as

$$\frac{\partial^2}{\partial \rho^2} \psi = 1 + \Delta - e^{-\psi}, \quad (55)$$

and solved subject to the boundary conditions $\psi(\rho=0)=0$ and $\frac{\partial \psi}{\partial \rho} \Big|_{\rho=0} = 0$. Here,

$$\Delta \equiv \frac{\gamma_b^3 \beta_b^2 c^2 k_{\beta 0}^2}{\hat{\omega}_p^2} - 1, \quad (56)$$

$\rho \equiv x/(\gamma_b \lambda_D)$ is a scaled x coordinate, and $\lambda_D \equiv [T/(m\hat{\omega}_p^2)]^{1/2}$ and $\hat{\omega}_p \equiv [q^2 \hat{n}/(\epsilon_0 m)]^{1/2}$ denote the Debye length and plasma frequency formed from the peak (on-axis) density scale \hat{n} and temperature T . The parameter $\Delta \in (0, \infty)$ is a positive, dimensionless parameter relating the ratio of applied to space-charge defocusing forces and is analogous to the scaled parameter commonly employed in analysis of 2D thermal equilibrium beams and non-neutral plasmas [21,38]. A particular choice of gamma factors has been made so that T corresponds to the (non-relativistic) kinetic temperature defined in the boosted beam frame [16,21].

The transformed Poisson equation (55) is highly non-linear and must, in general, be solved numerically for ψ . The numerical solution is illustrated in Fig. 2, where the normalized density

$$\mathcal{N}(\rho) \equiv \frac{n(\rho)}{\hat{n}} = \exp(-\psi) \quad (57)$$

is plotted versus $\rho = x/(\gamma_b \lambda_D)$ for values of Δ covering several decades. Only positive ρ is shown because $n(\rho) = n(-\rho)$. For small values of Δ , the scaled density \mathcal{N} varies little from unity from $\rho = 0$ until intermediate-to-large values of ρ [corresponding to a large number of Debye lengths, since $\rho = x/(\gamma_b \lambda_D)$], where \mathcal{N} rapidly falls to exponentially small values as ρ increases by 4–5 units (i.e., Debye lengths). The width in ρ of the x -falloff varies little with Δ , whereas the edge of the flat, central region scales as $\rho_{\text{edge}} = 2.3 \log_{10}(\Delta)$. The extreme flatness of \mathcal{N} when $\Delta \ll 1$ leads to numerical precision problems when directly integrating Eq. (55) for ψ using standard numerical methods. Because of this, the numerical solution is constructed by transforming Eq. (55) for $\delta \mathcal{N} = 1 - \mathcal{N} = 1 - \exp(-\psi)$ and then numerically solving for $\delta \mathcal{N}(\rho)$ out to near the beam edge where $\delta \mathcal{N}$ starts varying rapidly,

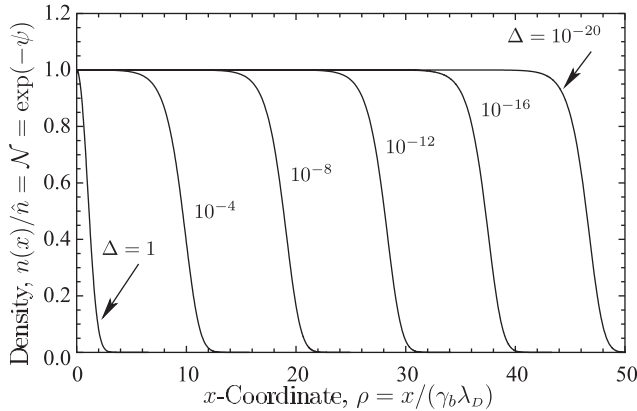


FIG. 2. Scaled density $\mathcal{N} = n(\rho)/\hat{n} = \exp(-\psi)$ plotted versus the scaled x coordinate $\rho = x/(\gamma_b \lambda_D)$ calculated from the solution of the transformed thermal equilibrium Poisson equation (55) for indicated values of Δ .

and then the solution is continued from this near-edge point until \mathcal{N} becomes exponentially small by directly integrating the transformed Poisson equation (55). This procedure rapidly generates accurate solutions for arbitrarily small values of Δ without use of special high precision numerical methods. Details of this numerical procedure are given in Ref. [39]. For $\Delta \gg 1$, $e^{-\psi} \ll 1 + \Delta$ and Eq. (55) can be analytically solved to show that

$$\psi \simeq \frac{1 + \Delta}{2} \rho^2, \quad \mathcal{N} = e^{-\psi} \simeq e^{-(1+\Delta)\rho^2/2}, \quad (58)$$

thereby showing, consistently with results in Fig. 2, that the x -density profile $\mathcal{N}(\rho)$ becomes Gaussian in what will be shown to correspond to the warm beam limit. Approximate, closed form analytical solutions for $\Delta \ll 1$ can also be constructed using methods presented for the cylindrical beam cases in Refs. [21,38].

For modeling applications the sheet-beam thermal distribution parameters \hat{n} and T , or equivalently,

$$T^* \equiv \frac{T}{m\gamma_b \beta_b^2 c^2}, \quad (59)$$

should be related to standard parameters applied in accelerator physics such as focusing strength ($k_{\beta 0}$), rms emittance (ϵ), and perveance (P) in addition to particle parameters q , m , β_b , and γ_b . Similarly, the scaled equilibrium parameter Δ can be better interpreted when cast in terms of the relative space-charge strength of an rms-equivalent beam. To derive equations of constraint to implement this parameter conversion, first from Eq. (56)

$$\hat{n} = \frac{\epsilon_0 m \gamma_b^3 \beta_b^2 c^2 k_{\beta 0}^2}{q^2 (1 + \Delta)}. \quad (60)$$

Using this result, we have

$$(\gamma_b \lambda_D)^2 = (1 + \Delta) \frac{T^*}{k_{\beta 0}^2}, \quad (61)$$

and the integrated density N can be expressed as

$$\begin{aligned} N &= \int_{-\infty}^{\infty} dx n \\ &= \frac{2\epsilon_0 m \gamma_b^3 \beta_b^2 c^2 k_{\beta 0}}{q^2} \sqrt{\frac{T^*}{1 + \Delta}} \int_0^{\infty} d\rho \mathcal{N}, \end{aligned} \quad (62)$$

and the perveance P [Eq. (30)] can be expressed as

$$P = \frac{q^2 N}{2\epsilon_0 m \gamma_b^3 \beta_b^2 c^2} = k_{\beta 0} \sqrt{\frac{T^*}{1 + \Delta}} \int_0^{\infty} d\rho \mathcal{N}. \quad (63)$$

This perveance expression is also useful when recast as

$$T^* = \left(\frac{P}{k_{\beta 0}} \right)^2 \frac{1 + \Delta}{\left(\int_0^{\infty} d\rho \mathcal{N} \right)^2}. \quad (64)$$

Similarly, from the definition of the rms-edge emittance ε [Eq. (31)] reduces to

$$\varepsilon^2 = 9\langle x^2 \rangle \langle x'^2 \rangle$$

with the moments $\langle x^2 \rangle$ and $\langle x'^2 \rangle$ calculated directly from the distribution as

$$\langle x^2 \rangle = \frac{1 + \Delta}{k_{\beta 0}^2} T^* \frac{\int_0^\infty d\rho \rho^2 \mathcal{N}}{\int_0^\infty d\rho \mathcal{N}}, \quad \langle x'^2 \rangle = T^*, \quad (65)$$

and T^* is eliminated using Eq. (64) to obtain

$$\varepsilon^2 = \frac{P^4}{k_{\beta 0}^6} 9(1 + \Delta)^3 \frac{\int_0^\infty d\rho \rho^2 \mathcal{N}}{(\int_0^\infty d\rho \mathcal{N})^5}. \quad (66)$$

The emittance expression (66) can be alternatively recast as the constraint

$$\frac{k_{\beta 0}^3 \varepsilon}{P^2} = 3(1 + \Delta)^{3/2} \frac{(\int_0^\infty d\rho \rho^2 \mathcal{N})^{1/2}}{(\int_0^\infty d\rho \mathcal{N})^{5/2}}. \quad (67)$$

Because the right-hand side (rhs) of this equation is a function of Δ and $k_{\beta 0}^3 \varepsilon / P^2$ is a ratio of accelerator parameters, Eq. (67) can be applied as a nonlinear integral constraint fixing the scaled equilibrium parameter Δ . Alternatively, the tune depression $\sigma/\sigma_0 \in (0, 1)$ of a matched rms-equivalent beam can be calculated to interpret the value of Δ for the thermal equilibrium sheet beam. Equation (39) is applied to calculate σ/σ_0 using $x_b = \sqrt{3\langle x^2 \rangle}$ as

$$\begin{aligned} \frac{\sigma}{\sigma_0} &= \left[1 - \frac{P}{\sqrt{3} k_{\beta 0}^2 \sqrt{\langle x^2 \rangle}} \right]^{1/2} \\ &= \left[1 - \frac{1}{\sqrt{3}(1 + \Delta)} \frac{(\int_0^\infty d\rho \mathcal{N})^{3/2}}{(\int_0^\infty d\rho \rho^2 \mathcal{N})^{1/2}} \right]^{1/2}. \end{aligned} \quad (68)$$

Here, we employ Eqs. (63) and (65) to calculate the ratio $P/(k_{\beta 0}^2 \sqrt{\langle x^2 \rangle})$ as a function of Δ . Equation (68) is numerically evaluated to plot Δ as a function of $\sigma/\sigma_0 \in (0, 1)$ in Fig. 3. From this plot it is evident that space-charge dominated beams with small values of σ/σ_0 are modeled by thermal equilibria with extremely small values of Δ .

The constraints in Eqs. (60)–(68) are applied to clarify changes in the sheet-beam equilibrium as space-charge intensity varies in Fig. 4. The density profile $n(x)$ and contours of the phase-space distribution $f(x, x')$ are plotted for a constrained scale equilibrium with $P/k_{\beta 0} = \text{const}$ and are illustrated as the relative space-charge strength (as measured by rms-equivalent beam σ/σ_0) is varied. These plots can be interpreted as showing how an equilibrium with fixed focusing strength ($k_{\beta 0} = \text{const}$) and charge (i.e., perveance $P = \text{const}$) varies in structure as the temperature (or equivalently, T^*) or phase-space area (i.e., emittance ε) is varied. In Fig. 4(a) the scaled density is plotted for $x > 0$. The corresponding kinetic temperature is spatially uniform

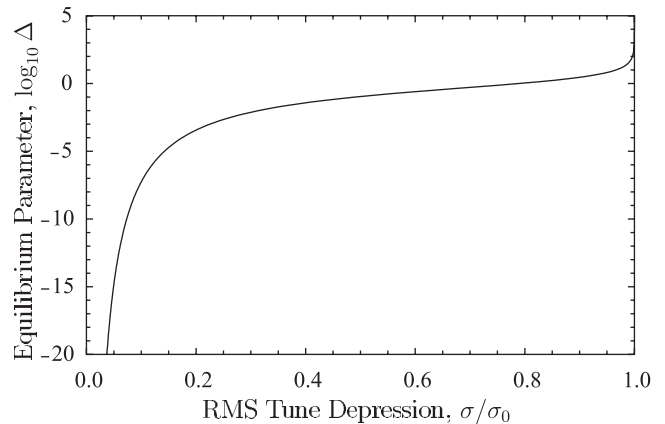


FIG. 3. Dimensionless thermal equilibrium parameter $\Delta = \gamma_b^3 \beta_b^2 c^2 k_{\beta 0}^2 / \omega_p^2 - 1$ plotted versus rms-equivalent beam tune depression σ/σ_0 as calculated from Eq. (68).

with value $T_x = T = \text{const}$. Contours of the scaled distribution $f(H)/f(0)$ are shown in Figs. 4(b)–4(d) for high, intermediate, and low values of σ/σ_0 (or space-charge intensity). Scaled parameters for the thermal equilibrium solution presented in Fig. 4 are given in Table II. Parameters are divided into scale independent ones applicable to any physical scale with the corresponding value of σ/σ_0 (or Δ), and parameters dependent on the specific value of $P/k_{\beta 0}$ employed in Fig. 4. In Table II, $x_b = \sqrt{3\langle x^2 \rangle}$ denotes an rms measure of the beam half-width. Results presented in Fig. 4 are very similar to 2D thermal equilibrium beam results presented in Appendix F of Ref. [21]. Note from the development in Sec. II C that, if the goal is to choose the best sheet-beam equivalent parameters to higher-dimensional systems, the parameters (including $P/k_{\beta 0}$) should be adjusted for the particular operating point set by the charge, emittance, and focusing strength. For example, the continuous focusing equivalency condition (51) could be applied. For simplicity of presentation, this optimized equivalence detail is neglected in Fig. 4.

Figure 4(a) illustrates how the thermal equilibrium density profile sharpens and becomes more step-function-like with increasing relative space-charge strength (i.e., small σ/σ_0 , or equivalently, small T^*), and consistent with the limiting form in Eq. (58) becomes Gaussian-like for weak space-charge strength (i.e., $\sigma/\sigma_0 \sim 1$, or equivalently large T^*). The peak density \hat{n} increases with increasing space-charge strength, while the statistical beam edge $x_b = \sqrt{3\langle x^2 \rangle}$ decreases with increasing space-charge strength. The extreme flatness of the density profile as the beam cools can be understood as resulting from strong Debye screening of the linear applied focusing force. Properties of Debye screening in the sheet-beam model are detailed in Sec. III B. Contrasting Figs. 4(b)–4(d), note for weak space-charge that the phase-space contours are nearly elliptical indicating nearly linear dynamics with the applied

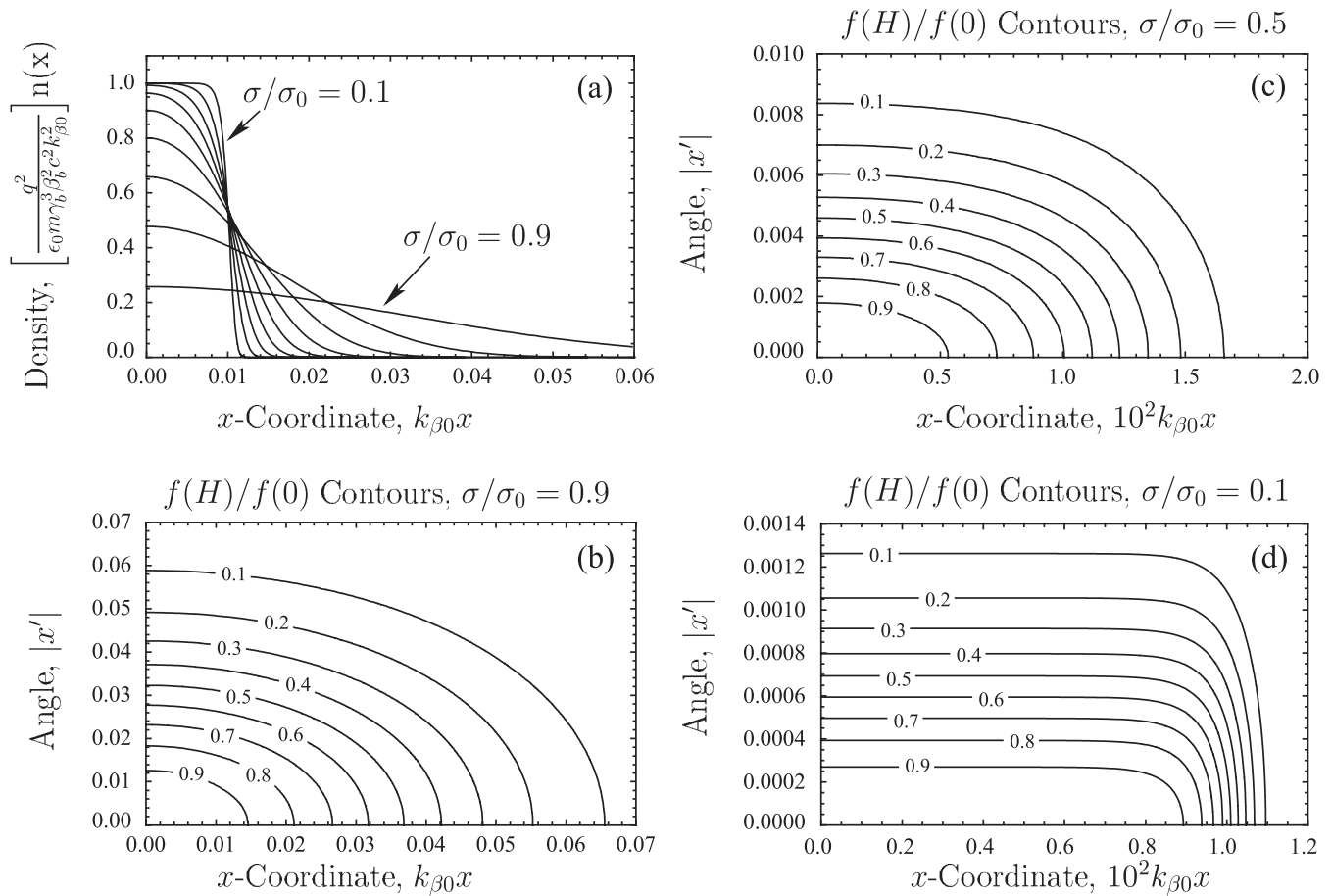


FIG. 4. Thermal equilibrium distribution for a constrained scale set by $P/k_{\beta 0} = 0.02$. In (a) the scaled density profile $[q^2/(\epsilon_0 m \gamma_b^3 \beta_b^2 c^2)]n(x)$ is plotted versus the dimensionless x coordinate $k_{\beta 0}x$ for rms-equivalent beam space-charge strengths $\sigma/\sigma_0 = 0.9, 0.8, \dots, 0.1$. In (b), (c), and (d), normalized distribution contours $f(H)/f(0) = \text{const}$ are plotted as a function of $k_{\beta 0}x$ and x' for $\sigma/\sigma_0 = 0.9, 0.5$, and 0.1 . Contours are labeled by the value of $f(H)/f(0)$. Values of σ/σ_0 correspond to the equilibrium parameters in Table II. Panels are ordered to allow direct contrasts with Fig. 19 in Ref. [21].

focusing field dominating. In this situation, one expects particle oscillation frequencies close to the frequency that particles oscillate in the (linear) applied focusing field. In contrast, for strong space-charge, the phase-space contours

(note the large change in the scale of the axes) become approximately rectangular indicating nearly force-free particle motion deep within the beam core until particles enter the edge region where a strong nonlinear force transition

TABLE II. Dimensionless parameters for a sheet-beam thermal equilibrium presented in Fig. 4 calculated for specified values of σ/σ_0 . Scale independent parameters applicable to any physical size thermal equilibrium and scale dependent parameters employed for the specific choice equilibrium employed in Fig. 4 are grouped in separate columns to the left and right.

σ/σ_0	Δ	Scale independent		Scale dependent with $\frac{P}{k_{\beta 0}} = 0.01$			
		$(k_{\beta 0}^3 \epsilon)/P^2$	$(k_{\beta 0}^2 x_b^2)/[T/(m \gamma_b \beta_b^2 c^2)]$	$k_{\beta 0} \gamma_b \lambda_D$	$\frac{T}{m \gamma_b \beta_b^2 c^2}$	$k_{\beta 0} x_b$	$k_{\beta 0} \epsilon$
0.9	2.879	24.99	3.686	5.399×10^{-2}	7.515×10^{-4}	0.052 63	2.499×10^{-3}
0.8	1.093	6.204	4.641	1.866×10^{-2}	1.663×10^{-4}	0.027 78	6.204×10^{-4}
0.7	0.5181	2.712	6.027	9.841×10^{-3}	6.379×10^{-5}	0.019 61	2.712×10^{-4}
0.6	0.2500	1.481	8.157	6.117×10^{-3}	2.993×10^{-5}	0.015 63	1.481×10^{-4}
0.5	0.1097	0.9009	11.68	4.109×10^{-3}	1.522×10^{-5}	0.013 33	9.009×10^{-5}
0.4	3.780×10^{-2}	0.5757	18.18	2.844×10^{-3}	7.794×10^{-6}	0.011 90	5.757×10^{-5}
0.3	7.562×10^{-3}	0.3681	32.29	1.941×10^{-3}	3.740×10^{-6}	0.010 99	3.681×10^{-5}
0.2	3.649×10^{-4}	0.2201	72.91	1.220×10^{-3}	1.488×10^{-6}	0.010 42	2.201×10^{-5}
0.1	5.522×10^{-8}	0.1030	294.6	5.885×10^{-4}	3.463×10^{-7}	0.010 10	1.030×10^{-5}

effectively reflects the particle back towards the core. In this situation, one expects a broad spectrum of amplitude-dependent particle oscillation frequencies. The particle frequency distribution is explicitly calculated in Sec. III C and results verify this interpretation.

B. Debye screening

Paralleling Davidson's 2D analysis carried out in the non-neutral plasma case [23,33] which is directly applicable to continuously focused beams, we show that the 1D sheet-beam thermal equilibrium distribution described in Sec. III A produces the same characteristic Debye screening of applied perturbations as found in 2D and 3D geometries. This similarity of results between the 1D sheet beam and more physical, higher-dimensional models occurs in spite of the radically different long-range structure of the Coulomb interaction in 1D. One expects that similar Debye screening of perturbations leads to similar collective effects, thereby supporting the idea that the simple sheet-beam model can be applied to better understand strong space-charge effects.

First, consider a "test" sheet charge placed at the origin ($x = 0$) with charge density $\rho = \Sigma_t \delta(x)$. Here, $\Sigma_t = \text{const}$ is the surface charge density representing the test sheet charge and $\delta(x)$ is a Dirac-delta function. The solution of the 1D Poisson equation in free space, $\frac{\partial^2}{\partial x^2} \phi = -\frac{\rho}{\epsilon_0}$, gives the "bare" electric field

$$-\frac{\partial \phi}{\partial x} = \text{sgn}(x) \frac{\Sigma_t}{2\epsilon_0}. \quad (69)$$

Next, we consider the total potential ϕ produced by the test sheet charge inserted in a thermal equilibrium sheet beam which is assumed to adiabatically adapt to the presence of the test charge. The Poisson equation describing this situation is

$$\frac{\partial^2}{\partial x^2} \phi = -\frac{q}{\epsilon_0} \int_{-\infty}^{\infty} dx' f(H) - \frac{\Sigma_t}{\epsilon_0} \delta(x). \quad (70)$$

The parameter Σ_t can be made arbitrarily small for consistency with the assumption that the equilibrium is allowed to adiabatically adapt to the presence of the test charge. We expand the potential as

$$\phi = \phi_0 + \delta\phi, \quad (71)$$

where ϕ_0 is the equilibrium potential in the absence of the test charge and $\delta\phi$ is the perturbed potential from the test charge. The test charge is taken to be sufficiently small where $|\frac{q\delta\phi}{\gamma_b^2 T}| \ll 1$, and consistent with the adiabatic assumption, we have to leading order

$$\begin{aligned} n(x) &= \int_{-\infty}^{\infty} dx' f(H) = \hat{n} e^{-\psi} \simeq \hat{n} e^{-\psi_0(x)} e^{-q\delta\phi/(\gamma_b^2 T)} \\ &\simeq \hat{n} e^{-\psi_0(x)} \left(1 - \frac{q\delta\phi}{\gamma_b^2 T} \right). \end{aligned}$$

Here, $\psi_0 = \frac{1}{T} [\frac{1}{2} k_{\beta 0}^2 x^2 + \frac{q\phi_0}{m\gamma_b^3 \beta_b^2 c^2}]$. Using this leading-order expansion and the fact that ϕ_0 satisfies the thermal equilibrium Poisson equation (70) in the absence of the test charge ($\Sigma_t = 0$) yields the perturbed Poisson equation for $\delta\phi$:

$$\frac{\partial^2}{\partial x^2} \delta\phi \simeq \frac{q^2}{\epsilon_0 \gamma_b^2 T} \hat{n} e^{-\psi_0(x)} \delta\phi - \frac{\Sigma_t}{\epsilon_0} \delta(x). \quad (72)$$

We further assume a relatively cold beam equilibrium (i.e., $\Delta \ll 1$ and σ/σ_0 small). Then, consistent with the analysis in Sec. III A, the density is flat near the test charge (i.e., $\psi_0 \simeq 0$ and the forces from the equilibrium self-fields and the applied focusing approximately cancel each other) and we can then take

$$\hat{n} e^{-\psi_0(x)} \simeq \hat{n}. \quad (73)$$

Under these approximations, the Poisson equation (72) for the perturbed potential becomes

$$\frac{\partial^2}{\partial x^2} \delta\phi - \frac{\delta\phi}{(\gamma_b \lambda_D)^2} \simeq -\frac{\Sigma_t}{\epsilon_0} \delta(x) \quad (74)$$

with $\lambda_D = [\epsilon_0 T / (q^2 \hat{n})]^{1/2}$. The solution of Eq. (74) for $\delta\phi$ which is regular as $|x| \rightarrow \infty$ is

$$\delta\phi(x) \simeq \frac{\gamma_b \lambda_D \Sigma_t}{2\epsilon_0} e^{-|x|/(\gamma_b \lambda_D)}, \quad (75)$$

and the corresponding electric field is

$$-\frac{\partial \delta\phi}{\partial x} \simeq \text{sgn}(x) \frac{\Sigma_t}{2\epsilon_0} e^{-|x|/(\gamma_b \lambda_D)}. \quad (76)$$

The solutions in Eqs. (75) and (76) for the potential and electric field produced by the screened test charge are valid out to values of x near the edge of the beam where $n(x)$ varies significantly from \hat{n} .

Comparing Eqs. (69) and (76) for the bare and screened electric field of the test charge, note that screening

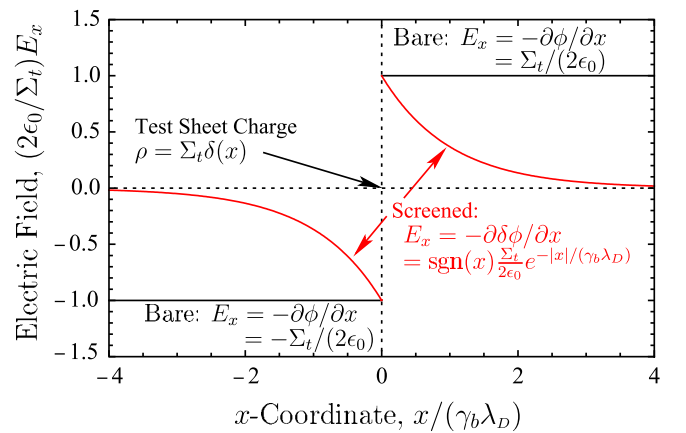


FIG. 5. Contrast of the bare (black) and screened (red) electric field of a test sheet charge inserted at $x = 0$ in a thermal equilibrium sheet beam.

TABLE III. Form of the screened potential produced by a test charge inserted in a continuously focused thermal equilibrium beam distribution in 1D, 2D, and 3D models. Here, $\lambda_t = \text{const}$ is line-density of a test charge in 2D, $q_t = \text{const}$ is the charge of the test charge in 3D, and the Debye length $\lambda_D = [\epsilon_0 T / (q^2 \hat{n})]^{1/2}$ is defined the same in 1D, 2D, and 3D.

Dimension	Distance measure	Test charge density $\rho =$	Screened potential $\delta\phi \approx$
1D	$ x $	$\sum_t \delta(x)$	$\frac{\gamma_b \lambda_D \sum_t}{2\epsilon_0} e^{- x /(\gamma_b \lambda_D)}$
2D	$r = \sqrt{x^2 + y^2}$	$\lambda_t \frac{\delta(r)}{2\pi r}$	$\frac{\lambda_t}{2\sqrt{2\pi}\epsilon_0} \frac{r}{\sqrt{r/(\gamma_b \lambda_D)}} e^{-r/(\gamma_b \lambda_D)}, r \gg \gamma_b \lambda_D$
3D	$r = \sqrt{x^2 + y^2 + z^2}$	$q_t \delta(x)\delta(y)\delta(z)$	$\frac{q_t}{4\pi\epsilon_0 r} e^{-r/(\gamma_b \lambda_D)}$

provided by the sheet-beam equilibrium results in the bare electric field produced by the test charge being exponentially damped in terms of the distance from the test charge in relativistic Debye lengths $\gamma_b \lambda_D$. The bare and screened electric fields are contrasted in Fig. 5. As summarized in Table III, this classic 1D Debye screening exponential factor has the same form in terms of the variation of the exponential damping factor of the potential $\delta\phi$ with distance from the test charge as is found (approximate form) in 2D and (exact form) in 3D [40]. This equivalence in Debye screening characteristics between the 1D, 2D, and 3D models occurs in spite of the radically different form of the Coulomb field in the three cases. As in the 2D and 3D systems, the screened interaction in 1D does not require overall charge neutrality and beam particles redistribute to screen the bare free-space field produced by the test charge. Because the collective screening properties in 1D have the same characteristic scaling as in higher-dimensional models, one expects similar collective effects in the sheet-beam model relative to the more physical, higher-dimensional models. This supports the use of simpler-to-solve sheet-beam models to guide intuition on collective effects. Use of radically different models having similar Debye screening properties is considered an underlying reason why simpler, lower-dimensional numerical simulations can represent processes in physical systems of higher dimensions [41].

The sheet-beam Debye screening result also lends physical insight on why the density profile n is extremely flat at high space-charge intensity for a wide variety of choices of $f(H)$ corresponding to smooth, self-consistent equilibrium distributions [see, for example, the 1D thermal choice in Sec. III A, and 2D choices in Appendices D–F of Ref. [21] for waterbag, parabolic, and thermal forms]. Space-charge adapts to screen out the linear applied focusing force (leading to a uniform density profile since a uniform density profile produces linear self-field forces) until distances far enough from the center are reached where there is insufficient charge in the equilibrium to further screen the applied focusing force, after which the density rapidly falls to low values with an edge shape characteristic of the specific equilibrium distribution function $f(H)$. For the thermal equilibrium sheet beam, the smooth edge density profile rapidly falling off to exponentially small values is the result of the smooth exponential dependence in

Eq. (52). If desired, the analysis presented above can be extended by not taking the uniform density approximation in Eq. (73) and/or changing the position of the test charge in the equilibrium [$\sum_t \delta(x) \rightarrow \sum_t \delta(x - x_t)$ with $x = x_t$ the position of the test sheet charge] to study how the Debye screening is modified as the test charge approaches the edge of the beam and/or space-charge becomes weak.

C. Distribution of particle oscillation frequencies

In accelerator physics, particle oscillation frequencies are of fundamental interest. Effects are often interpreted in terms of resonances between characteristic particle oscillation frequencies and (periodic) applied and self-field produced perturbations acting on the beam. Therefore, it is important to understand how the distribution of particle oscillation frequencies changes due to intense self-field effects. Historically speaking, space-charge effects have often been interpreted with uniform density “KV”-type distributions which produce linear self-field forces that are more amenable to analytic analysis. In such a KV description of beams, all particles internal to the core distribution have the same characteristic oscillation frequency regardless of the amplitude of their oscillations. Consequently, the KV model can predict strong resonances and pronounced instability. Such results are often at odds with simulations and laboratory experiments with more physical, smooth distributions which have a spectrum of oscillation amplitude-dependent frequencies and both lesser degrees of instability and lesser consequences thereof due to low saturation amplitudes. Here, we extend results first presented in Appendix A of Ref. [8] and employ the sheet-beam model with a thermal equilibrium distribution to show that strong space-charge results in a broad distribution of particle oscillation frequencies consistent with expectations of enhanced stability. Implications of results are broadly discussed.

First, consider a sheet beam in a continuous focusing channel with $\kappa = k_{\beta 0}^2 = \text{const}$ without an aperture (free space) and an unspecified equilibrium distribution $f(H)$. For any particle in the distribution, $H = \frac{1}{2}x'^2 + \frac{1}{2}k_{\beta 0}^2 x^2 + \frac{q\phi}{m\gamma_b^3 \beta_b^2 c^2} = \text{const}$. The value of H can be taken as a measure of the particle oscillation amplitude and the number of particles with a particular value of H is determined by

the value of $f(H)$. Methods analogous to those presented in Ref. [42] can be applied to show that the continuously focused equilibrium potential is necessarily symmetric with $\phi(x) = \phi(-x)$. Using these results, the wavelength λ of a full cycle of the closed particle orbit in the 1D equilibrium can be expressed as

$$\lambda = \oint_{\text{orbit}} ds = 2^{3/2} \int_0^{x_t} \frac{dx}{\sqrt{H - (\frac{1}{2}k_{\beta 0}^2 x^2 + \frac{q\phi}{m\gamma_b^3 \beta_b^2 c^2})}}, \quad (77)$$

where $x = x_t > 0$ is the turning point of the orbit (i.e., $x = x_t$ corresponds to $x' = 0$ and $x'' < 0$) which satisfies the constraint

$$\frac{1}{2}k_{\beta 0}^2 x_t^2 - \frac{q\phi(x = x_t)}{m\gamma_b^3 \beta_b^2 c^2} = H. \quad (78)$$

Here, without loss of generality, we have assumed a potential reference $\phi(x = 0) = 0$ so that $H > 0$ for all particles. Use of an action-angle formulation [43] with $J = \oint_{\text{orbit}} dx x'$ and $\lambda = \partial J / \partial H$ produces an identical formula to evaluate as the direct calculation leading to Eq. (77).

It is convenient to denote the depressed wave number of the particle oscillation by

$$k_{\beta} \equiv \frac{2\pi}{\lambda}. \quad (79)$$

In the absence of beam space-charge ($P \rightarrow 0$), all particles, regardless of the value of H , have the same undepressed wave number of particle oscillations under the action of the linear applied focusing force, i.e.,

$$\lim_{P \rightarrow 0} k_{\beta} = k_{\beta 0} \equiv \frac{2\pi}{\lambda_0} = \text{const.} \quad (80)$$

We measure the relative particle oscillation wave number by

$$\frac{k_{\beta}}{k_{\beta 0}} = \frac{\lambda_0}{\lambda} = \frac{2\pi}{(k_{\beta 0} \lambda)}. \quad (81)$$

The value of $k_{\beta}/k_{\beta 0}$ will depend on the value of H in the particle distribution $f(H)$. Because space-charge is defocusing and cancels out part of the applied focusing force over the orbit cycle, particles oscillate less rapidly in the presence of space-charge ($P > 0$), and we have $\lambda \geq \lambda_0$ (with the equality holding for $P = 0$) and $k_{\beta}/k_{\beta 0} \in [0, 1]$. Thus, $k_{\beta}/k_{\beta 0}$ provides an easy-to-interpret, scale independent, normalized measure of spatial oscillation frequency in the distribution $f(H)$.

For a sheet-beam thermal equilibrium, some straightforward analysis using the results of Sec. III A shows that Eqs. (77) and (78) can be expressed in scaled dimensionless form as

$$(k_{\beta 0} \lambda) = 2^{3/2} \sqrt{1 + \Delta} \int_0^{\rho_t} \frac{d\rho}{\sqrt{\tilde{H} - \psi}}, \quad (82)$$

and

$$\psi(\rho = \rho_t) = \tilde{H}. \quad (83)$$

Here, $\rho_t = x_t/(\gamma_b \lambda_D)$ is the scaled turning point of the orbit, and

$$\tilde{H} \equiv \frac{m\gamma_b \beta_b^2 c^2}{T} H = \frac{H}{T^*} \quad (84)$$

is the scaled Hamiltonian.

Several limits of Eq. (82) can be simply calculated and are useful to help verify numerical calculations. First, for $\Delta \gg 1$, Eq. (58) can be applied for ψ to calculate $\rho_t = \sqrt{2\tilde{H}/(1 + \Delta)}$ and show that

$$\begin{aligned} (k_{\beta 0} \lambda)|_{\Delta \gg 1} &\approx 2^{3/2} \sqrt{1 + \Delta} \\ &\times \int_0^{\sqrt{2\tilde{H}/(1+\Delta)}} \frac{d\rho}{\sqrt{\tilde{H} - (1 + \Delta)\rho^2/2}} \\ &= 2\pi. \end{aligned} \quad (85)$$

This result shows that Eq. (82) is consistent with the required result that all particles oscillate with wavelength $\lambda = \lambda_0 = 2\pi/k_{\beta 0}$ in the applied focusing force when space-charge defocusing forces are negligible. Next, regardless of the value of Δ , for small-amplitude particle oscillations with $\tilde{H} \ll 1$ we calculate the limiting form of $(k_{\beta 0} \lambda)$. Taking $\psi \leq \tilde{H} \ll 1$, Eq. (55) can be solved to show that $\psi \approx \Delta \rho^2/2$ giving $\rho_t \approx \sqrt{2\tilde{H}/\Delta}$. Using these results in Eq. (82), the resulting integral can be calculated to show that

$$\lim_{\tilde{H} \rightarrow 0} (k_{\beta 0} \lambda) = 2\pi \sqrt{\frac{1 + \Delta}{\Delta}}, \quad (86)$$

thereby showing there is always a minimum oscillation frequency in the distribution with $\lim_{\tilde{H} \rightarrow 0} \frac{k_{\beta}}{k_{\beta 0}} = \lim_{\tilde{H} \rightarrow 0} \frac{2\pi}{k_{\beta 0} \lambda} = \sqrt{\frac{\Delta}{1 + \Delta}}$.

The distribution of particle oscillation frequencies calculated in an equilibrium can be more readily interpreted when cast in normalized form. For the sheet-beam thermal equilibrium, we define

$$F(\tilde{H}) \equiv \frac{f(\tilde{H})}{\int_0^{\infty} d\tilde{H} f(\tilde{H})} = e^{-\tilde{H}} \quad (87)$$

as a normalized [i.e., $\int_0^{\infty} d\tilde{H} F(\tilde{H}) = 1$] distribution with $F(\tilde{H})d\tilde{H}$ giving the fraction of particles with oscillation amplitude within $d\tilde{H}$ of \tilde{H} . Carrying out a probability transform from the variable \tilde{H} to $k_{\beta}/k_{\beta 0}$, we take $F(k_{\beta}/k_{\beta 0})d(k_{\beta}/k_{\beta 0}) = F(\tilde{H})d\tilde{H}$ and obtain

$$F(k_{\beta}/k_{\beta 0}) = \frac{e^{-\tilde{H}}}{\frac{d(k_{\beta}/k_{\beta 0})}{d\tilde{H}}} = -\frac{(k_{\beta 0} \lambda)^2 e^{-\tilde{H}}}{2\pi \frac{d(k_{\beta 0} \lambda)}{d\tilde{H}}}. \quad (88)$$

$F(k_\beta/k_{\beta 0})$ is the normalized [i.e., $\int_0^1 d(k_\beta/k_{\beta 0}) \times F(k_\beta/k_{\beta 0}) = 1$] distribution of relative oscillation frequencies in the beam with $F(k_\beta/k_{\beta 0})d(k_\beta/k_{\beta 0})$ giving the fraction of particles with relative frequencies within $d(k_\beta/k_{\beta 0})$ of $(k_\beta/k_{\beta 0})$.

We numerically generate plots of the normalized distribution of sheet-beam oscillation frequencies F as a function of $k_\beta/k_{\beta 0}$ for specified values of the thermal equilibrium parameter $\Delta = \gamma_b^3 \beta_b^2 c^2 k_{\beta 0}^2 / \hat{\omega}_p^2 - 1$ [Eq. (56)] as follows.

Step 1.—Using the formulation in Sec. III A, the solution for the effective potential $\psi(\rho)$ of the equilibrium is numerically calculated for specified Δ out to a sufficiently large cutoff value of ρ . \square

Step 2.—The scaled oscillation wavelength $(k_{\beta 0}\lambda)$ is calculated as a function of \tilde{H} using Eqs. (82) and (83) for discretized values of $\tilde{H} \in [0, \tilde{H}_{\max}]$. Here, \tilde{H}_{\max} is a sufficiently large cutoff value of \tilde{H} to resolve the “tail” of the distribution and the discretized values of \tilde{H} must generally be appropriately spaced to resolve features of the distribution. \square

Step 3.—The derivative $d(k_{\beta 0}\lambda)/d\tilde{H}$ is numerically calculated as a function of \tilde{H} using the discretized data in (2). \square

Step 4.—Equations (88) and (81) are applied to parametrically plot the frequency distribution $F(k_\beta/k_{\beta 0})$ versus $k_\beta/k_{\beta 0}$ using the discretized data points in \tilde{H} . \square

In this procedure we find that care must be taken in spacing discretized values of $\tilde{H} \in [0, \tilde{H}_{\max}]$ to achieve sufficient accuracy when calculating $d(k_{\beta 0}\lambda)/d\tilde{H}$. Points were taken with uniform increments in $\log \tilde{H}$ to concentrate resolution for small \tilde{H} with systematic spacing while still covering a large range with a reasonable number of points.

Results calculated from steps 1 and 2 of this procedure are presented in Fig. 6 where the normalized particle oscillation wavelength $\lambda/\lambda_0 = (k_{\beta 0}\lambda)/(2\pi)$ and frequency $k/k_{\beta 0} = \lambda_0/\lambda$ are plotted versus the transformed Hamiltonian \tilde{H} . Curves are shown for indicated values of rms-equivalent beam space-charge strength as measured by $\sigma/\sigma_0 \in (0, 1)$ (or equivalently, the equilibrium parameter Δ given in Table II). Properties of the thermal equilibrium distribution for these values of σ/σ_0 can be found in Sec. III A. Results are consistent with the weak space-charge limit in Eq. (85) as evident by the curve for λ/λ_0 in Fig. 6(a) with $\sigma/\sigma_0 = 0.9$ approaching unit value. Limiting values of λ/λ_0 and $k_\beta/k_{\beta 0}$ as $\tilde{H} \rightarrow 0$ are consistent with Eq. (86). Note from Fig. 6(b) that the frequency of particle oscillations k_β varies more over the indicated range of particle oscillation energy measured by \tilde{H} as the space-charge strength increases (i.e., smaller values of σ/σ_0).

Results obtained from steps 3 and 4 of the procedure to calculate the frequency distribution F versus normalized particle oscillation frequency $k_\beta/k_{\beta 0} \in (0, 1)$ are shown in Fig. 7. The curves are applicable to thermal equilibrium

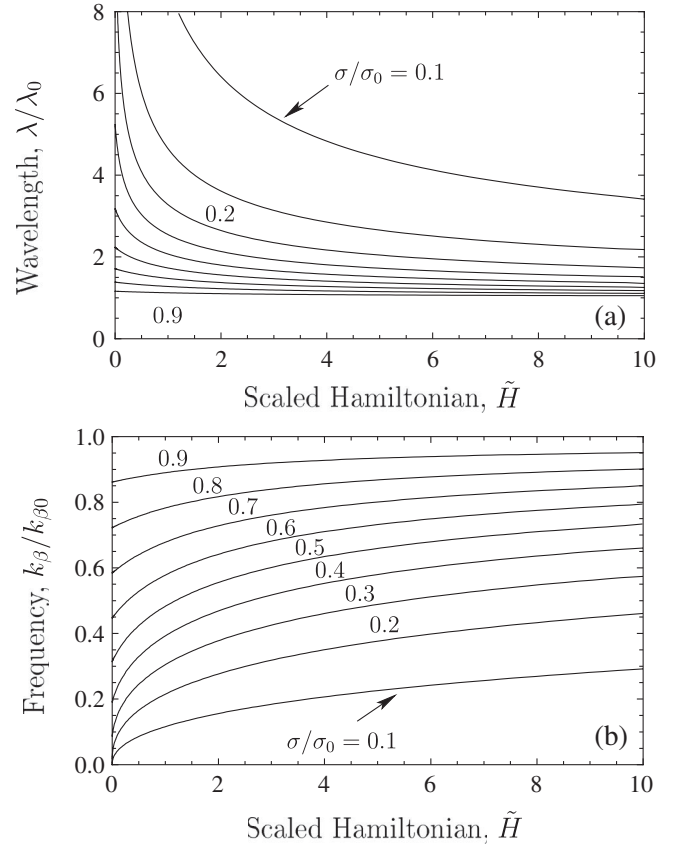


FIG. 6. Scaled particle oscillation wavelength $\lambda/\lambda_0 = (k_{\beta 0}\lambda)/(2\pi)$ (a) and oscillation frequency $k_\beta/k_{\beta 0} = \lambda_0/\lambda$ (b) versus dimensionless transformed Hamiltonian \tilde{H} . Shown for rms-equivalent beam space-charge strength $\sigma/\sigma_0 = 0.9, 0.8, 0.7, \dots, 0.1$. Scaled equilibrium parameters corresponding to σ/σ_0 are given in Table II.

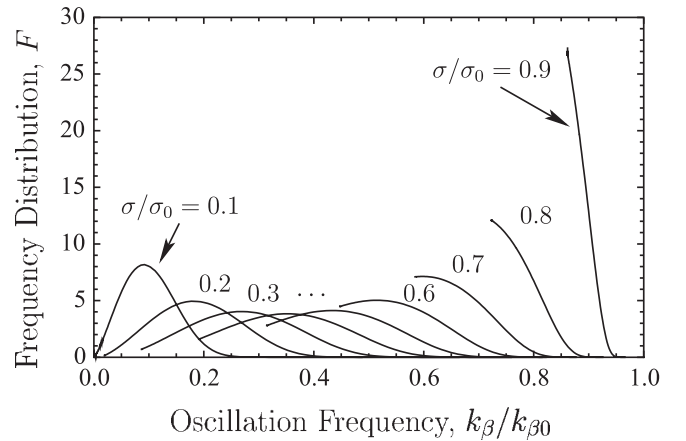


FIG. 7. Normalized frequency distribution F versus normalized particle oscillation frequency $k_\beta/k_{\beta 0}$ for the thermal equilibrium sheet beam. Shown for rms-equivalent beam space-charge strength $\sigma/\sigma_0 = 0.9, 0.8, 0.7, \dots, 0.1$. Corresponding Hamiltonian dependencies used to calculate the plot are given in Fig. 6. Statistical and extreme properties of the distribution curves are given in Table IV and quantities tabulated are illustrated graphically in Fig. 8.

TABLE IV. Statistical and extreme values of the frequency distribution F for the thermal equilibrium sheet-beam parameters plotted in Fig. 7. Values tabulated are illustrated graphically in Fig. 8.

σ/σ_0	Δ	Statistical measures				Extreme measures			
		Mean $\mu_F = \overline{k_\beta}/k_{\beta 0}$	rms $\sigma_F = \sqrt{k_\beta^2 - \overline{k_\beta}^2}/k_{\beta 0}$	Width $F_w = 2\sqrt{3}\sigma_F$	Relative width F_w/μ_F	At Max[F] F	$k_\beta/k_{\beta 0}$	At left F cutoff F	$k_\beta/k_{\beta 0}$
0.9	2.879	0.886	0.0176	0.0610	0.0689	27.3	0.862	27.3	0.862
0.8	1.093	0.774	0.0354	0.123	0.159	12.1	0.723	12.1	0.723
0.7	0.5181	0.663	0.0531	0.184	0.277	7.13	0.598	7.09	0.584
0.6	0.2500	0.557	0.0696	0.241	0.433	5.03	0.515	4.47	0.447
0.5	0.1097	0.456	0.0833	0.289	0.634	4.12	0.434	2.79	0.314
0.4	3.780×10^{-2}	0.361	0.0915	0.317	0.878	3.83	0.352	1.58	0.191
0.3	7.562×10^{-3}	0.274	0.0898	0.311	1.14	4.03	0.270	0.698	0.0866
0.2	3.649×10^{-4}	0.190	0.0750	0.260	1.37	4.94	0.177	0.153	0.0191
0.1	5.522×10^{-8}	0.102	0.0465	0.161	1.58	8.18	0.0912	0.00191	0.000235

distributions of arbitrary physical scale and illustrate changes over a broad range of relative space-charge strength. Table IV summarizes corresponding properties of the frequency distribution plots $F(k_\beta/k_{\beta 0})$. Statistical properties of F tabulated include: mean frequency (μ_F), rms frequency spread about the mean frequency (σ_F), frequency width measure (F_w), and relative frequency width (F_w/μ_F). These quantities are defined by

$$\text{mean: } \mu_F \equiv \overline{k_\beta}/k_{\beta 0},$$

$$\text{rms width: } \sigma_F \equiv \sqrt{(k_\beta - \overline{k_\beta})^2}/k_{\beta 0} = \sqrt{k_\beta^2 - \overline{k_\beta}^2}/k_{\beta 0},$$

$$\text{width measure: } F_w \equiv 2\sqrt{3}\sigma_F, \quad (89)$$

$$\text{relative width: } F_w/\mu_F.$$

Here, overlines denote averages with respect to the frequency distribution F , i.e.,

$$\overline{\dots} = \int_0^1 d(k_\beta/k_{\beta 0}) \dots F. \quad (90)$$

The $2\sqrt{3}$ coefficient multiplying the rms width σ_F in the definition of the statistical width measure σ_F is taken to

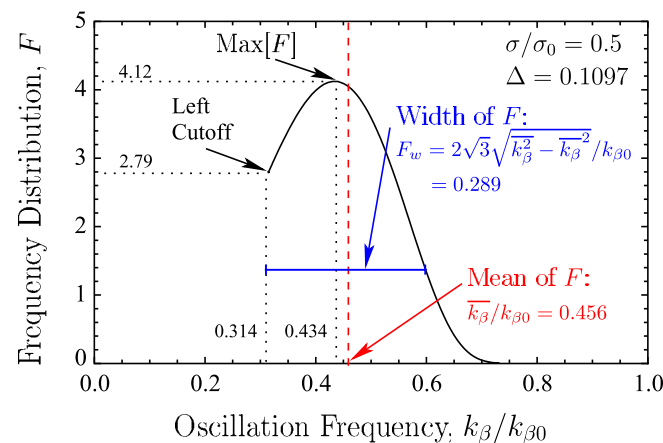


FIG. 8. Quantities listed in Table IV illustrated for $\sigma/\sigma_0 = 0.5$.

give a reasonable sense of the width of F in $k_\beta/k_{\beta 0}$ about $\overline{k_\beta}/k_{\beta 0}$. The factor is motivated by analogy to the 1D rms-equivalent sheet-beam discussion in Sec. II B. The relative width F_w/μ_F simply measures the frequency width (F_w) relative to the mean frequency (μ_F) to give a better sense of the effective spread in frequencies. Extreme measures of the distribution are also tabulated including the value of F and $k_\beta/k_{\beta 0}$ at the peak and left-edge cutoff of F . To aid interpretation, quantities tabulated are illustrated in Fig. 8 for $F(k_\beta/k_{\beta 0})$ shown for the midrange value $\sigma/\sigma_0 = 0.5$.

To better understand the parametric variations of the frequency distribution F illustrated in Fig. 7 and Table IV, first note that for σ/σ_0 corresponding to weaker rms-equivalent beam space-charge (i.e., nearer the $\sigma/\sigma_0 = 0.9$ case), F is sharply peaked with relatively small width in $k_\beta/k_{\beta 0}$. As space-charge becomes stronger (reduced σ/σ_0), the distribution becomes broader in width and more smoothly varying relative to the $\sigma/\sigma_0 = 0.9$ case. Regardless of the value of $\sigma/\sigma_0 \in (0, 1)$, there is *always* a lower bound value of $k_\beta/k_{\beta 0} > 0$ at the left of the distribution. This value is consistent with the $\tilde{H} \rightarrow 0$ limit value calculated from Eqs. (86) and occurs because for finite σ/σ_0 Debye screening does not result in a perfectly flat density profile within the core of the beam with an appropriate value where the space-charge defocusing force will cancel the linear applied focusing force. However, for very strong space-charge (see $\sigma/\sigma_0 = 0.1, 0.2$ curves and corresponding table entries) this minimum value of $k_\beta/k_{\beta 0}$ is very close to zero because the density profile in the core is exceedingly flat from almost complete Debye screening of the linear applied focusing field. Conversely, for weak space-charge (see the $\sigma/\sigma_0 = 0.8, 0.9$ curves and table entries) the density profile deep within the core of the beam is near Gaussian shaped and there is only limited cancellation of the applied focusing strength. In all cases, the frequency distribution F is an asymmetric function of $k_\beta/k_{\beta 0}$ about the mean frequency (i.e., $k_\beta/k_{\beta 0} = \overline{k_\beta}/k_{\beta 0}$). The average normalized frequency $k_\beta/k_{\beta 0}$ is *not* generally equal to the rms-equivalent beam tune depression σ/σ_0

(i.e., $\overline{k_\beta}/k_{\beta 0} \neq \sigma/\sigma_0$), though the difference becomes substantially less for both relatively weak (see $\sigma/\sigma_0 = 0.9$) and strong (see $\sigma/\sigma_0 = 0.1$) space-charge than for the broad middle range of σ/σ_0 (see $\sigma/\sigma_0 = 0.8$ – 0.3). Also, both the peak value and left cutoff of F closely coincide for weaker space-charge (same values to the precision tabulated for $\sigma/\sigma_0 = 0.9, 0.8$) but shift significantly as space-charge becomes stronger. In both the extreme limits of weak ($\sigma/\sigma_0 \rightarrow 1$) and strong ($\sigma/\sigma_0 \rightarrow 0$) space-charge, F becomes a Dirac-delta function with unit area under the curve but infinite height and zero width. However, properties of the delta-function representation are very different in the weak and strong space-charge limits. In the weak case, the distribution is one-sided with zero width with mean frequency $\overline{k_\beta}/k_{\beta 0} \rightarrow 1$. In the strong case, the mean frequency goes to zero ($\overline{k_\beta} \rightarrow 0$) while the spread relative to the mean appears to remain broad as the limit is approached (i.e., F_w/μ_F large). Note from Table IV that the frequency width relative to the mean frequency (i.e., the relative width F_w/μ_F) appears to monotonically increase with increasing space-charge strength (decreasing σ/σ_0).

The parametric results for distribution of particle oscillation frequencies in the sheet-beam thermal equilibrium likely have properties in common with a wide variety of smooth, continuously focused sheet-beam distributions. Here we conclude this section with a point discussion on such similarities, together with a more speculative point discussion on the extent to which features found for the continuously focused sheet-beam thermal distribution might extrapolate to provide guidance for periodically focused systems in higher dimensions and resulting implications for transport and stability of beams with intense space-charge. By nature, these point discussions are more speculative than the systematic developments presented up to this point. It is hoped that this discussion can help stimulate future research.

Point 1.—Many features illustrated for the thermal equilibrium distribution including the sharp left cutoff of the frequency distribution F in $k_\beta/k_{\beta 0}$ and both the approximate scaling of rms distribution width F_w and relative width F_w/μ_F in $k_\beta/k_{\beta 0}$ are likely to persist for other choices of equilibrium sheet-beam distributions $f(H)$ that are reasonably smooth. However, the shape of the tail of F for high values of $k_\beta/k_{\beta 0}$ is likely to vary with the specific form of the distribution. Distributions with a maximum H cutoff in $f(H)$ will have a corresponding, upper-bound value of $k_\beta/k_{\beta 0}$ where $F \rightarrow 0$. This contrasts the situation for the thermal distribution where F smoothly reduces to exponentially small values as $k_\beta/k_{\beta 0}$ becomes larger. Procedures introduced in this paper to calculate the equilibrium structure (see Sec. III A) and the corresponding distribution of particle oscillation frequencies F for the thermal equilibrium distribution can be straightforwardly adapted to other continuously focused equilibrium

distributions $f(H)$. Specific examples of other equilibria with significantly different phase-space structures include 1D sheet-beam equilibria analogous to the 2D continuous focusing waterbag and parabolic equilibria presented in Appendices D and E in Ref. [21]. \square

Point 2.—The broad distribution of particle oscillation frequencies found for strong space-charge is not surprising given the equilibrium structure plots presented in Sec. III A. When space-charge is weak, particle oscillation frequencies are only slightly depressed from the oscillation frequency in the linear applied focusing force which is independent of the amplitude of oscillation. But as space-charge defocusing becomes strong, Debye screening in the core of the beam leads to a flat density profile with a nearly linear space-charge defocusing force which almost cancels the applied focusing, resulting in nearly force-free motion within the core. Particles with large enough oscillation amplitude enter the edge of the beam and the applied focusing force overwhelms the rapidly dropping space-charge force and reflects the particles within a few Debye lengths. Thus, for stronger space-charge, the frequency of particle oscillation becomes strongly dependent on amplitude (as measured by the transformed Hamiltonian \tilde{H}) as evident from the low σ/σ_0 curves in Fig. 6(b). \square

Point 3.—The statistical width F_w (or equivalently, the rms width σ_F) of the frequency distribution F for a thermal equilibrium sheet beam appears broadest for $\sigma/\sigma_0 \sim 0.4$ but remains relatively broad over a wide range of strong space-charge—including the extreme case shown with $\sigma/\sigma_0 = 0.1$. To the extent this broad parametric width is preserved for other relatively smooth, but nonthermal, near-equilibrium and rms-matched beam distributions, this width helps clarify why space-charge dominated beams have been observed in laboratory experiments and simulations appear to have robust stability to internal modes [44–46]. Although the single-particle frequencies do not simply correspond to collective mode frequencies, the spectrum of frequencies of the equilibrium beam strongly influences collective mode properties. This can be understood from the method of characteristics [18,19,23], which shows that small-amplitude mode perturbations evolve according to a linear operator acting along characteristic orbits in the equilibrium. Thus, the spectrum of single-particle frequencies in the equilibrium can strongly impact collective mode properties. Generally speaking, one expects a broader distribution of frequencies in the equilibrium to result in a lesser degree of instability with both smaller growth rates and smaller unstable parameter regions with lower saturation amplitudes for unstable perturbations. \square

Point 4.—Vlasov simulations of 2D transversely continuously focused beams support the point made above, that beams with strong space-charge exhibit a high degree of stability. Initial rms envelope-matched 2D beams having highly nonuniform density and/or kinetic temperature

profiles are found to rapidly relax with little net emittance growth or envelope mismatch even for very strong space-charge strength [47]. Such results suggest a broad underlying spectrum of particle and wave oscillation frequencies in beams with strong space-charge even when the initial distribution is far from equilibrium form. Similar results are found in periodic quadrupole focusing channels [48]. Effective relaxations of initial semi-Gaussian beam distributions resulting from phase mixing and nonlinear wave interactions are found in simulations to occur most rapidly for $\sigma/\sigma_0 \sim 0.5$ where results here suggest that the frequency spectrum is most broad [49]. \square

Point 5.—Simulations and theory show that, if beam stability is defined practically in terms of limited rms emittance growth and halo generation, then a wide variety of 2D initial distributions are stable when transported in a periodic quadrupole transport channel without errors regardless of space-charge intensity—so long as the applied focusing strength is $\sigma_0 \lesssim 85^\circ$ per lattice period [45,46]. Large rms emittance growth results from significant numbers of near-edge particles rapidly evolving outside the statistical edge (core) of the beam and rapidly increasing in oscillation amplitude due to interaction with matched envelope oscillations of the core beam, rather than from growth of collective modes internal to the core of the beam. Interior mode instabilities, if present, appear to saturate at low amplitudes with little consequence. Insofar as the continuously focused thermal equilibrium sheet beam can provide a model for particle orbits in a nonequilibrium periodic quadrupole focusing channel, results found here showing a broad range of particle oscillation frequencies in the core of beams with intense space-charge further support the relative lack of detrimental internal mode instability noted above. \square

Point 6.—It has been observed that the rms-equivalent KV distribution works well to model beams with smooth distributions and weak space-charge [50]. This occurs in spite of the expectation that in weak space-charge regimes smooth distribution beams should have nonuniform (Gaussian-like in the thermal equilibrium case) density profiles leading to *more nonlinear* space-charge forces. The frequency distribution plots of the smooth thermal distribution suggest why the smooth distribution can be well modeled by a KV distribution in spite of the (small) nonlinear self-field forces. As $\sigma/\sigma_0 \rightarrow 1$ the frequency distribution F becomes sharp with narrow rms width in k_β with $\overline{k_\beta}/k_{\beta 0} \approx \sigma/\sigma_0$. Thus, particle orbits in the smooth distribution should be well approximated by particles making up an rms-equivalent KV distribution in spite of the (small) nonlinear space-charge force being modeled by a linear force. This suggests that the KV model can be reliable to predict low-order collective mode resonances when space-charge intensity is relatively weak. In weak space-charge regimes spurious instabilities of the KV model associated with the singular KV distribution form

are less problematic: in 2D continuous focusing models, all KV modes are stable for $\sigma/\sigma_0 > 0.3985$ (see Appendix B of Ref. [51]). Recent experiments and simulations supporting the reliability of the KV model as an aid to interpret space-charge effects for relatively weak space-charge are presented in Ref. [9]. \square

Point 7.—Conversely to the weak space-charge case discussed in the point above, in the strong space-charge limit the KV model is expected to provide a poor approximation to smooth distributions. For thermal distributions this failure occurs in spite of the fact that for low values of σ/σ_0 the density profile is very uniform for many Debye lengths before rapidly falling to exponentially small values in a few Debye lengths at the beam edge (see Sec. III A). The broad range of particle frequencies in smooth distributions is expected to strongly modify the collective response, other than for lowest order (envelope) modes. The plethora of strongly unstable, higher-order KV modes [50,51] appears to be suppressed, or saturates at low amplitudes with little consequence, when equilibrium orbits no longer advect perturbations with a single characteristic frequency. Historically, sheet-beam model results with KV distributions were first applied by Sacherer [6] to analyze space-charge induced resonance effects in rings. Interpretations and extensions to higher dimensions presented by Baartman in Ref. [7] have also been influential. Present results suggest that extrapolating such KV model results for collective mode resonances may be questionable when applied to collective modes beyond lowest order when space-charge intensity is high. However, this does not imply that all KV model results are invalid. For example, lowest order linear (envelope) instability appears robust enough to extrapolate to other distributions [44–46]. Also, Startsev *et al.* [52–54] analyzed a robust low-order transverse-longitudinal collective instability by applying the method of characteristics using (single-frequency) KV orbit equilibrium characteristics with perturbation operators for a smooth (thermal) core distribution to estimate growth rates, and found good agreement with r - z Vlasov simulation results. \square

Point 8.—Because generally $\overline{k_\beta}/k_{\beta 0} \neq \sigma/\sigma_0$, it follows that the unique particle oscillation frequency in an rms-equivalent KV beam does *not* equal the average oscillator frequency in the thermal distribution. Similar deviations from rms equivalency are reasonable to expect for other smooth distributions and suggest caution in the application of rms-equivalent parameter interpretations. Notice from Table IV that for the thermal equilibrium sheet beam $\overline{k_\beta}/k_{\beta 0} < \sigma/\sigma_0$ for all values of σ/σ_0 except $\sigma/\sigma_0 = 0.1$ where the deviation is small. The deviation of $\overline{k_\beta}/k_{\beta 0}$ from σ/σ_0 approaches zero in both the weak ($\sigma/\sigma_0 \rightarrow 1$) and strong ($\sigma/\sigma_0 \rightarrow 0$) space-charge limits. \square

Point 9.—In recent studies by Dorf *et al.* in Refs. [55,56], x - and y -plane particle oscillation frequencies are calculated by spectral analysis of orbits in

continuous and periodically focused beams with unbunched thermal equilibrium core distributions. Characteristic widths and scaling of 2D frequency distributions agree well with the 1D sheet-beam model presented here, suggesting further that the sheet-beam model can be broadly applied. The primary difference between the 1D and 2D results appears to be that the sharp left cutoff in 1D becomes rounded in 2D, which is likely attributable to dimensional scaling of 2D volume measures folded into the distribution projection. Note also that in a 2D system with nonlinear space-charge forces, Floquet's theorem does not apply and particle orbits are not closed in the x or y planes, so phase advances (frequencies) are formally ill posed. However, nearly constant frequency distributions obtained by transforming long orbits suggest that for equilibrium like distributions frequency projections can be regarded as nearly stationary, which furthers correspondence to the 1D model results presented here. \square

Point 10.—Finally, it appears likely that halo properties should be significantly different in the sheet-beam model relative to higher-dimensional models. A large amplitude halo is primarily driven by the breathing envelope mode [57]. In the sheet-beam model, the lower frequency quadrupole envelope mode appears to be accurately represented [see Sec. II B and Eq. (43)], but the higher-frequency breathing mode is not supported. Furthermore, scaling of space-charge forces with distance outside the envelope of an rms-equivalent core is different in the sheet-beam model (constant) relative to higher-dimensional models (falloff with distance) [46]. Together these features likely result in different characteristic halo resonances in the sheet-beam model relative to higher-dimensional models. However, for nontenuous halo processes leading to space-charge induced transport limits as described in Refs. [45,46], it is possible that resulting stability thresholds due to a variety of collective processes driving a significant fraction of particles well outside the beam core may be similar in sheet-beam models, though the final saturated beam states could differ due to different halo resonances supported. \square

IV. CONCLUSIONS

A 1D sheet-beam model has been reviewed and extended in a manner intended to enable applications to a broad range of beam transport problems with intense space-charge. A full Vlasov model with and without finite geometry effects, as well as reduced centroid and envelope moment descriptions, were developed. Specific attention was paid to the choice of sheet-beam parameters appropriate to represent more realistic, higher-dimensional beam models. The reduced complexity of the 1D sheet-beam model enables significant analytical progress on a variety of difficult problems with self-consistent space-charge. The sheet-beam model also provides a simple framework

which can be exploited to evaluate advanced methods for direct Vlasov simulations.

The efficacy of the sheet-beam model was illustrated with solutions to several problems of fundamental interest. A sheet-beam thermal equilibrium distribution was developed in a continuous focusing model to provide an example of a realistic, smooth distribution function. The thermal equilibrium was thoroughly analyzed and shown to have remarkably similar properties to higher-dimensional models in terms of both the equilibrium structure and Debye screening properties of a test charge placed in the equilibrium. These results support the conclusion that the sheet-beam model can be applied to reliably model beam equilibria and collective waves that closely resemble those in higher-dimensional models. The simplicity of the 1D sheet-beam model was further exploited to explicitly calculate the self-consistent distribution of particle oscillation frequencies within the thermal equilibrium distribution. Results were presented in a manner which applies to any thermal equilibrium regardless of physical scale, and quantified how strong space-charge significantly broadens the distribution of particle oscillation frequencies. Because a broader distribution of frequencies is expected to have reduced consequences of resonances with perturbations, this result helps explain the robust stability to internal modes typically observed in beams with intense space-charge in both laboratory experiments and numerical simulations.

ACKNOWLEDGMENTS

The authors wish to thank O. Anderson, J. Barnard, E. Lee, H. Okamoto, and E. Startsev for useful discussions. M. Campos Pinto helped verify aspects of results reported with Vlasov simulations which are not included herein. This research was performed under the auspices of the U.S. Department of Energy at the Lawrence Livermore and Lawrence Berkeley National Laboratories under Contracts No. DE-AC52-07NA27344 and No. DE-AC02-05CH11231.

APPENDIX A: SYSTEM ENERGY CONSERVATION CONSTRAINT

For continuous focusing with $\kappa = k_{\beta 0}^2 = \text{const}$, the Vlasov equation (14) can be operated on with $\int_{x_{pl}}^{x_{pr}} dx \int_{-\infty}^{\infty} dx' \frac{1}{2} x'^2 \dots$ and the boundary conditions $f(x = x_{pl}, x_{pr}) = 0$ applied to the result to show that

$$\begin{aligned} & \frac{\partial}{\partial s} \int_{x_{pl}}^{x_{pr}} dx \int_{-\infty}^{\infty} dx' \frac{1}{2} x'^2 f \\ & - \int_{x_{pl}}^{x_{pr}} dx \int_{-\infty}^{\infty} dx' \left(k_{\beta 0}^2 x + \frac{q}{m \gamma_b^3 \beta_b^2 c^2} \frac{\partial \phi}{\partial x} \right) \frac{x'}{2} \frac{\partial f}{\partial x'} = 0. \end{aligned} \quad (\text{A1})$$

Similarly, the continuity equation

$$\frac{\partial}{\partial s} n + \frac{\partial}{\partial x} \int_{-\infty}^{\infty} dx' x' f = 0 \quad (\text{A2})$$

is derived as usual by operating on the Vlasov equation with $\int_{-\infty}^{\infty} dx' \dots$ and applying the boundary condition $f(x' \rightarrow \pm\infty) = 0$ to the result. The continuity equation (A2) and the Poisson equation (3) with $n = \int_{-\infty}^{\infty} dx' f$ can then be applied together with partial integration to express Eq. (A1) as

$$\begin{aligned} & \frac{\partial}{\partial s} \left\{ \int_{x_{pl}}^{x_{pr}} dx \int_{-\infty}^{\infty} dx' \left(\frac{1}{2} x'^2 + \frac{1}{2} k_{\beta 0}^2 x'^2 \right) f \right. \\ & \quad \left. + \frac{\epsilon_0}{2m\gamma_b^3 \beta_b^2 c^2} \int_{x_{pl}}^{x_{pr}} dx \left| \frac{\partial \phi}{\partial x} \right|^2 \right\} \\ & = \frac{\epsilon_0}{m\gamma_b^3 \beta_b^2 c^2} \phi \frac{\partial}{\partial s} \frac{\partial \phi}{\partial x} \Big|_{x=x_{pl}}^{x=x_{pr}}. \end{aligned} \quad (\text{A3})$$

The terms within $\{\dots\}$ in Eq. (A3) can be identified (in order expressed) with the usual scaled ‘‘kinetic,’’ applied focusing potential, and electric field energies of the bounded 1D system. The term on the rhs of Eq. (A3) is related to the scaled energy flow provided by an external power source required to impose potentials $\phi = \phi_l, \phi_r$ on the plates at $x = x_{pl}, x_{pr}$. If $\phi_l = \text{const}$ and $\phi_r = \text{const}$, the s derivative can be moved through ϕ_l and ϕ_r to obtain

$$\phi \frac{\partial}{\partial s} \frac{\partial \phi}{\partial x} \Big|_{x=x_{pl}}^{x=x_{pr}} = \frac{\partial}{\partial s} \left[\phi_r \frac{\partial \phi}{\partial x} \Big|_{x=x_{pr}} - \phi_l \frac{\partial \phi}{\partial x} \Big|_{x=x_{pl}} \right]. \quad (\text{A4})$$

Equations (A3) and (A4) immediately imply the energy conservation constraint given in Eq. (21). Further clarification of the external source term in Eq. (21) is achieved by applying the field solution in Eq. (10) to show that

$$\begin{aligned} & \phi_r \frac{\partial \phi}{\partial x} \Big|_{x=x_{pr}} - \phi_l \frac{\partial \phi}{\partial x} \Big|_{x=x_{pl}} \\ & = \frac{(\phi_r - \phi_l)^2}{x_{pr} - x_{pl}} + \frac{q(\phi_r - \phi_l)}{\epsilon_0(x_{pr} - x_{pl})} \int_{x_{pl}}^{x_{pr}} dx N_x + \frac{qN\phi_r}{\epsilon_0}. \end{aligned} \quad (\text{A5})$$

Because ϕ_l, ϕ_r , and N are constants and the geometry is fixed, Eqs. (A4) and (A5) show that we can replace

$$\begin{aligned} & \frac{\epsilon_0}{m\gamma_b^2 \beta_b^2 c^2} \left[\phi_r \frac{\partial \phi}{\partial x} \Big|_{x=x_{pr}} - \phi_l \frac{\partial \phi}{\partial x} \Big|_{x=x_{pl}} \right] \\ & \rightarrow \frac{q(\phi_r - \phi_l)}{m\gamma_b^2 \beta_b^2 c^2 (x_{pr} - x_{pl})} \int_{x_{pl}}^{x_{pr}} dx N_x \end{aligned} \quad (\text{A6})$$

in Eq. (21) because the new term differs from the replaced term by a constant. This replacement explicitly shows that the external source term can be eliminated when $\phi_l = \phi_r = \text{const}$ because it is a constant (replacement term vanishes). The physical interpretation of this result is that the plate bias does not matter when the left and right plates are connected—as must be the case on the physical basis. Similarly, if $\phi_l = \phi_r \neq \text{const}$, Eq. (10) can be applied to show that $\phi \frac{\partial}{\partial s} \frac{\partial \phi}{\partial x} \Big|_{x=x_{pl}}^{x=x_{pr}} = 0$ and consequently the

conservation Eq. (21) can be applied in this case with no external source term. If desired, the field solution in Eq. (10) can be applied to recast the field energy $\frac{\epsilon_0}{2} \int_{x_{pl}}^{x_{pr}} dx \left| \frac{\partial \phi}{\partial x} \right|^2$ in Eq. (21) in explicit form.

APPENDIX B: FIELD-ENERGY EMITTANCE RELATION

Under the assumption of a symmetric beam with $n(x) = n(-x)$ focused within a symmetric geometry with $x_{pr} = -x_{pl} = x_p$ with no bending ($\phi_r = \phi_l = \text{const}$), the field resolution in Eq. (11) has only a direct (free-space) component. In this case, $\tilde{x} = x, \tilde{x}' = x', N_x = -\frac{\epsilon_0}{q} \frac{\partial \phi}{\partial x} + \frac{N}{2}$, and Eq. (44) can be expressed as

$$\frac{d}{ds} \epsilon^2 = -\frac{18q}{m\gamma_b^3 \beta_b^2 c^2} \left[\langle x^2 \rangle \left\langle x' \frac{\partial \phi}{\partial x} \right\rangle - \langle xx' \rangle \left\langle x \frac{\partial \phi}{\partial x} \right\rangle \right]. \quad (\text{B1})$$

For notational simplicity in this reduced geometry, we denote

$$N_x^s \equiv \int_0^x d\tilde{x} n(\tilde{x}) = N_x - \frac{N}{2}, \quad (\text{B2})$$

so that $-\frac{\partial \phi}{\partial x} = \frac{q}{\epsilon_0} N_x^s$ and express the self-field energy per unit area as

$$W = \frac{\epsilon_0}{2} \int_{-x_p}^{x_p} dx \left| \frac{\partial \phi}{\partial x} \right|^2 = \frac{q^2}{\epsilon_0} \int_0^{x_p} dx (N_x^s)^2. \quad (\text{B3})$$

Following Anderson in Ref. [10], some manipulations then show that the field moments in Eq. (B1) can be expressed as

$$\begin{aligned} \left\langle x \frac{\partial \phi}{\partial x} \right\rangle & = -\frac{1}{qN} \left(\frac{q^2 N^2 x_p}{4\epsilon_0} - W \right), \\ \left\langle x' \frac{\partial \phi}{\partial x} \right\rangle & = -\frac{1}{qN} \frac{d}{ds} \left(\frac{q^2 N^2 x_p}{4\epsilon_0} - W \right). \end{aligned} \quad (\text{B4})$$

The $\langle x \frac{\partial \phi}{\partial x} \rangle$ moment in Eq. (B4) is straightforward to calculate using Eq. (23) to show that $\langle x \frac{\partial \phi}{\partial x} \rangle = -\frac{2q}{\epsilon_0 N} \int_0^{x_p} dx x N_x^s n$ and then applying $n = \frac{\partial N_x^s}{\partial x}$ and partial integration. The $\langle x' \frac{\partial \phi}{\partial x} \rangle$ moment can be obtained by first directly calculating $\frac{dW}{ds} = \frac{2q^2}{\epsilon_0} \int_0^{x_p} dx N_x^s \frac{\partial N_x^s}{\partial s}$. Then $\frac{\partial N_x^s}{\partial s}$ in this expression is recast by first operating on the Vlasov equation (14) with $\int_{-\infty}^{\infty} dx' \dots$ to derive the continuity equation $\frac{\partial n}{\partial s} + \frac{\partial}{\partial x} (\int_{-\infty}^{\infty} dx' x' f) = 0$, after which the continuity equation is integrated for the symmetric density profile to first show that $\frac{\partial N_x^s}{\partial s} = -\int_{-\infty}^{\infty} dx' x' f$. Using this expression and adding $\frac{q^2 N^2 x_p}{4\epsilon_0} = \text{const}$ within the s derivative then obtains the given result. The field moments (B4) are then inserted in Eq. (45) and $\frac{d}{ds} \langle x^2 \rangle = 2 \langle xx' \rangle$ is applied to obtain

$$\begin{aligned} \frac{d}{ds} \varepsilon^2 &= \frac{18}{Nm\gamma_b^3 \beta_b^2 c^2} \left(\langle x^2 \rangle \frac{dW_F}{ds} - \langle xx' \rangle W_F \right) \\ &= \frac{18}{Nm\gamma_b^3 \beta_b^2 c^2} \langle x^2 \rangle^{3/2} \frac{d}{ds} \left(\frac{W_F}{\langle x^2 \rangle^{1/2}} \right), \end{aligned} \quad (\text{B5})$$

with $W_F \equiv \frac{q^2 N^2 x_p}{4\epsilon_0} - W$ [Eq. (46)], thereby deriving Eq. (45).

-
- [1] J. H. Booske, M. A. Basten, and A. H. Kumbasar, *Phys. Plasmas* **1**, 1714 (1994).
- [2] M. A. Basten and J. H. Booske, *J. Appl. Phys.* **85**, 6313 (1999).
- [3] B. E. Carlsten, *Phys. Plasmas* **9**, 5088 (2002).
- [4] B. E. Carlsten, L. M. Earley, W. B. Haynes, F. L. Krawczyk, F. P. Romero, S. J. Russell, E. I. Smirnova, and Z.-F. Wang, *IEEE Trans. Nucl. Sci.* **34**, 2393 (2006).
- [5] J. H. Booske, *Phys. Plasmas* **15**, 055502 (2008).
- [6] F. J. Sacherer, Ph.D. thesis, University of California, 1968.
- [7] R. Baartman, in *Workshop on Space Charge Physics in High Intensity Rings, Shelter Island, NY, 1998*, edited by A. U. Luccio and W.-T. Weng, AIP Conf. Proc. No. 448 (American Institute of Physics, New York, 1998), p. 56.
- [8] H. Okamoto and K. Yokoya, *Nucl. Instrum. Methods Phys. Res., Sect. A* **482**, 51 (2002).
- [9] S. Ohtsubo, M. Fujioka, H. Higaki, K. Ito, H. Okamoto, H. Sugimoto, and S. M. Lund, *Phys. Rev. ST Accel. Beams* **13**, 044201 (2010).
- [10] O. A. Anderson, *Part. Accel.* **21**, 197 (1987).
- [11] O. A. Anderson, *Nuovo Cimento Soc. Ital. Fis. A* **106**, 1605 (1993).
- [12] E. A. Startsev and R. C. Davidson, *Phys. Rev. ST Accel. Beams* **6**, 044401 (2003).
- [13] H. Okamoto, *Nucl. Instrum. Methods Phys. Res., Sect. A* **332**, 1 (1993).
- [14] R. C. Davidson, H. Qin, S. I. Tzenov, and E. A. Startsev, *Phys. Rev. ST Accel. Beams* **5**, 084402 (2002).
- [15] Various model results in this section and in Sec. III were verified with direct Vlasov simulation methods carried out by M. Campos Pinto using a multilevel particle method with adaptive reconstructions. Descriptions of the method and benchmark results will be submitted for publication.
- [16] M. Reiser, *Theory and Design of Charged Particle Beams* (Wiley, New York, 1994).
- [17] S. M. Lund and B. Bukh, *Phys. Rev. ST Accel. Beams* **7**, 024801 (2004).
- [18] J. J. Barnard and S. M. Lund, in U.S. Particle Accelerator School courses: Lawrence Livermore National Laboratory Report No. LLNL-AR-407617; Lawrence Berkeley National Laboratory Report No. LBNL-1097E; Lawrence Livermore National Laboratory Report No. UCRL-TM-231628; Lawrence Berkeley National Laboratory Report No. LBNL-62783; Lawrence Livermore National Laboratory Report No. UCRL-TM-203655; Lawrence Berkeley National Laboratory Report No. LBNL-54926; Lawrence Berkeley National Laboratory Report No. LBNL-49286.
- [19] J. J. Barnard and S. M. Lund, *Interaction of Intense Charged Particle Beams* (University of California at Berkeley, Berkeley, CA, Spring Semester 2009).
- [20] H. Wiedemann, *Particle Accelerator Physics I: Basic Principles and Linear Beam Dynamics* (Springer-Verlag, New York, 2004), 2nd ed.
- [21] S. M. Lund, T. Kikuchi, and R. C. Davidson, *Phys. Rev. ST Accel. Beams* **12**, 114801 (2009).
- [22] R. C. Davidson and H. Qin, *Physics of Intense Charged Particle Beams in High Energy Accelerators* (World Scientific, New York, 2001).
- [23] R. C. Davidson, *Physics of Nonneutral Plasmas* (Addison-Wesley, Reading, MA, 1990), re-released (World Scientific, Singapore, 2001).
- [24] R. C. Davidson, *Phys. Rev. Lett.* **81**, 991 (1998).
- [25] T. K. Fowler, *J. Math. Phys. (N.Y.)* **4**, 559 (1963).
- [26] I. Kapchinskij and V. Vladimirskij, in *Proceedings of the International Conference on High Energy Accelerators and Instrumentation* (CERN Scientific Information Service, Geneva, 1959), p. 274.
- [27] E. D. Courant and H. S. Snyder, *Ann. Phys. (N.Y.)* **3**, 1 (1958).
- [28] P. M. Lapostolle, *IEEE Trans. Nucl. Sci.* **18**, 1101 (1971).
- [29] P. M. Lapostolle, CERN Technical Report No. CERN-ISR-DI/71-6, 1971.
- [30] E. P. Lee, S. S. Yu, and W. A. Barletta, *Nucl. Fusion* **21**, 961 (1981).
- [31] T. Wangler, K. Crandall, R. Mills, and M. Reiser, *IEEE Trans. Nucl. Sci.* **32**, 2196 (1985).
- [32] H. Wiedemann, *Particle Accelerator Physics II: Nonlinear and Higher-Order Beam Dynamics* (Springer-Verlag, New York, 2004), 2nd ed.
- [33] R. C. Davidson, *J. Plasma Phys.* **6**, 229 (1971).
- [34] See Ref. [23] and references therein.
- [35] D. H. E. Dubin and T. M. O'Neil, *Rev. Mod. Phys.* **71**, 87 (1999), and references therein.
- [36] J. D. Lawson, *The Physics of Charged-Particle Beams* (Clarendon Press, Oxford, 1977).
- [37] See Ref. [16] and references therein.
- [38] E. A. Startsev and S. M. Lund, *Phys. Plasmas* **15**, 043101 (2008).
- [39] S. M. Lund and G. Bazouin, in *Proceedings of the 2011 Particle Accelerator Conference*, New York City, NY, 2011, WEP099.
- [40] Analysis of Debye screening in a single species non-neutral plasma confined in traps can be immediately applied to continuously focused beams as a beam-frame equivalent system. 2D non-neutral plasma treatments can be found in Refs. [23,33]. Beam analyses can be found in lecture notes by Barnard and Lund from the U.S. Particle Accelerator School [18] and the University of California at Berkeley [19].
- [41] C. K. Birdsall and A. B. Langdon, *Plasma Physics via Computer Simulation* (McGraw-Hill, New York, 1985).
- [42] S. M. Lund, *Phys. Rev. ST Accel. Beams* **10**, 064203 (2007).
- [43] H. Goldstein, *Classical Mechanics* (Addison Wesley, Reading, MA, 1980), 2nd ed.
- [44] M. G. Tiefenback, Ph.D. thesis, University of California at Berkeley, 1986.

- [45] S. M. Lund and S. R. Chawla, *Nucl. Instrum. Methods Phys. Res., Sect. A* **561**, 203 (2006).
- [46] S. M. Lund, J. J. Barnard, B. Bukh, S. R. Chawla, and S. H. Chilton, *Nucl. Instrum. Methods Phys. Res., Sect. A* **577**, 173 (2007).
- [47] S. M. Lund, D. P. Grote, and R. C. Davidson, *Nucl. Instrum. Methods Phys. Res., Sect. A* **544**, 472 (2005).
- [48] Unpublished Vlasov simulations by Lund and Grote find similar conclusions in periodic FODO (focus-drift-defocus-drift) quadrupole channels to those made on the collective relaxation of perturbations in a continuous focusing channel in Ref. [47] *provided* that the applied focusing has phase advance $\sigma_0 \lesssim 85^\circ$ per lattice period. Relaxations also appear more rapid and complete, likely due to a larger spectrum of frequencies in the periodic relative to the continuous focusing case. The focusing strength limit of $\sigma_0 \lesssim 85^\circ$ results from processes detailed in Refs. [45,46].
- [49] S. M. Lund, J. J. Barnard, and J. Miller, in *Proceedings of the 1995 Particle Accelerator Conference, Dallas, TX* (IEEE, Piscataway, NJ, 1995), p. 3278.
- [50] I. Hofmann, L. J. Laslett, L. Smith, and I. Haber, *Part. Accel.* **13**, 145 (1983).
- [51] S. M. Lund and R. C. Davidson, *Phys. Plasmas* **5**, 3028 (1998).
- [52] E. A. Startsev, R. C. Davidson, and H. Qin, *Phys. Plasmas* **9**, 3138 (2002).
- [53] E. A. Startsev and R. C. Davidson, *Phys. Rev. ST Accel. Beams* **6**, 084401 (2003).
- [54] E. A. Startsev and R. C. Davidson, *Phys. Plasmas* **10**, 4829 (2003).
- [55] M. A. Dorf, R. C. Davidson, and E. A. Startsev (to be published).
- [56] M. A. Dorf, Ph.D. thesis, Princeton University, 2010.
- [57] R. L. Gluckstern, *Phys. Rev. Lett.* **73**, 1247 (1994).